Remote Sensing of Environment 216 (2018) 311–327

Contents lists available at ScienceDirect

Remote Sensing of Environment

journal homepage: www.elsevier.com/locate/rse

PhotoSpec: A new instrument to measure spatially distributed red and far-red Solar-Induced Chlorophyll Fluorescence

Katja Grossmann[a,b], Christian Frankenberg[c,d], Troy S. Magney[c,d], Stephen C. Hurlock[a,b], Ulrike Seibt[a], Jochen Stutz[a,b,*]

[a] Department of Atmospheric and Oceanic Sciences, University of California Los Angeles, Los Angeles, CA, USA
[b] Joint Institute for Regional Earth System Science and University of California Los Angeles, Los Angeles, CA, USA
[c] Division of Geological and Planetary Sciences, California Institute of Technology, Pasadena, CA, USA
[d] NASA Jet Propulsion Laboratory, California Institute of Technology, Pasadena, CA, USA

ARTICLE INFO

Keywords:
Solar-Induced Chlorophyll Fluorescence (SIF)
Photosynthesis
Remote sensing

ABSTRACT

Solar-Induced Chlorophyll Fluorescence (SIF) is an emission of light in the 650–850 nm spectral range from the excited state of the chlorophyll-a pigment after absorption of photosynthetically active radiation (PAR). As this is directly linked to the electron transport chain in oxygenic photosynthesis, SIF is a powerful proxy for photosynthetic activity. SIF observations are relatively new and, while global scale measurements from satellites using high-resolution spectroscopy of Fraunhofer bands are becoming more available, observations at the intermediate canopy scale using these techniques are sparse.

We present a novel ground-based spectrometer system - PhotoSpec - for measuring SIF in the red (670–732 nm) and far-red (729–784 nm) wavelength range as well as canopy reflectance (400–900 nm) to calculate vegetation indices, such as the normalized difference vegetation index (NDVI), the enhanced vegetation index (EVI), and the photochemical reflectance index (PRI). PhotoSpec includes a 2D scanning telescope unit which can be pointed to any location in a canopy with a narrow field of view (FOV = 0.7°). PhotoSpec has a high signal-to-noise ratio and spectral resolution, which allows high precision solar Fraunhofer line retrievals over the entire fluorescence wavelength range under all atmospheric conditions using a new two-step linearized least-squares retrieval procedure.

Initial PhotoSpec observations include the diurnal SIF cycle of single broad leaves, grass, and dark-light transitions. Results from the first tower-based measurements in Costa Rica show that the instrument can continuously monitor SIF of several tropical species throughout the day. The PhotoSpec instrument can be used to explore the relationship between SIF, photosynthetic efficiencies, Gross Primary Productivity (GPP), and the impact of canopy radiative transfer, viewing geometry, and stress conditions at the canopy scale.

1. Introduction

Solar-Induced Chlorophyll Fluorescence (SIF) is defined as the re-emission of de-excited photons in chlorophyll-a generated by incident radiation from the sun. The chlorophyll fluorescence emission spectrum ranges from around 650 nm to 850 nm and includes two broadband peaks centered in the red (685 nm) and far-red (740 nm) wavelength range (e.g., Genty et al., 1989; Krause and Weis, 1991; Baker, 2008; Porcar-Castell et al., 2014). SIF emitted from vegetation can be used as a constraint for photosynthetic activity and is a powerful proxy for the estimation of Gross Primary Production (GPP) and to study terrestrial ecosystems and the carbon cycle (e.g., Frankenberg et al., 2011b; Zhang et al., 2016; Du et al., 2017; Sun et al., 2017).

SIF is observable on a global scale from space (Frankenberg et al., 2011a,b, 2012; Joiner et al., 2011, 2012b; Guanter et al., 2012, 2013) from spectra recorded by the Greenhouse Gas Observing Satellite (GOSAT) (Frankenberg et al., 2011b; Joiner et al., 2011), the SCanning Imaging Absorption SpectroMeter for Atmospheric CHartographY (SCIAMACHY) (Joiner et al., 2012b; Wolanin et al., 2015), the Global Ozone Monitoring Experiment (GOME-2) (Joiner et al., 2013) as well as NASA's Orbiting Carbon Observatory-2 (OCO-2) satellite (Frankenberg et al., 2014; Sun et al., 2017, 2018). Progress has been made in applying satellite SIF data to study large-scale terrestrial ecosystem dynamics (e.g., Lee et al., 2013; Guanter et al., 2013; Zhang et al., 2014; Köhler

* Corresponding author.
E-mail address: jochen@atmos.ucla.edu (J. Stutz).

https://doi.org/10.1016/j.rse.2018.07.002
Received 30 November 2017; Received in revised form 19 June 2018; Accepted 2 July 2018

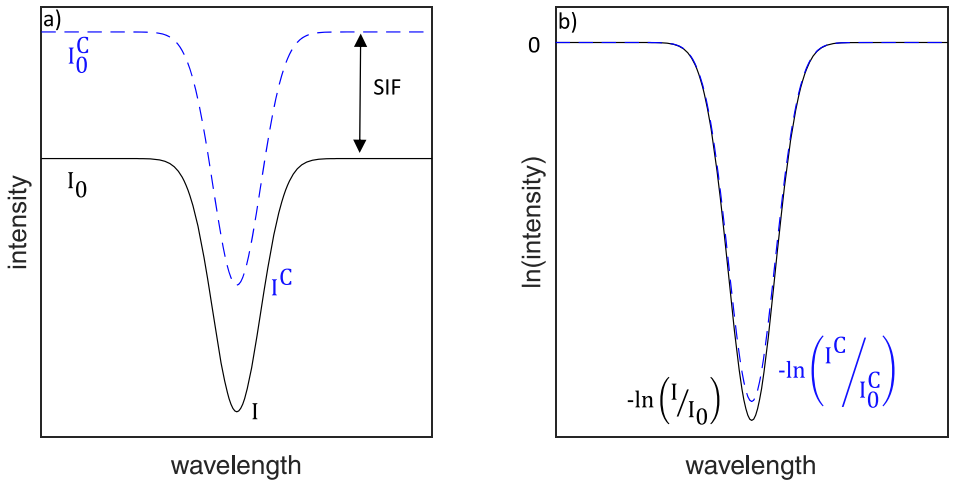

Fig. 1. Principle of SIF retrievals using Fraunhofer line in-filling. Panel a) shows the change in intensity of a Fraunhofer line, I_0 and I. For clarity, we chose the canopy reflectivity $a^C = 1$ to calculate the canopy intensities I_0^C and I^C. Panel b) shows the same bands as $-\ln(I/I_0)$ and $-\ln(I^C/I_0^C)$.

et al., 2015; Sun et al., 2015), but it is still uncertain to what extent variations of SIF and GPP relate to each other at increasing scales (e.g., Porcar-Castell et al., 2014).

Recently, spectrometer systems have been developed to retrieve SIF from above-canopy towers, unmanned aerial vehicles (UAVs), or aircraft to link leaf to global scale data (e.g., Moya et al., 1998, 2004; Meroni et al., 2009; Rascher et al., 2009; Guanter et al., 2013; Burkart et al., 2014; Rascher et al., 2015; Cogliati et al., 2015a; Middleton et al., 2017; Du et al., 2017). For example, measurements of canopy SIF at 760 nm were performed in temperate deciduous forests by using the spectrometer system FluoSpec (Yang et al., 2015, 2017). The ground-based MRI and SFLUOR box instruments were used to measure SIF and vegetation indices of different canopies such as sugar beet, grassland, or a lawn carpet (Cogliati et al., 2015a). Rossini et al. (2015) measured red and far-red fluorescence using the airborne imaging spectrometer HyPlant over a grass carpet treated with an herbicide.

SIF observations above the canopy are still sparse and require different instrumental design criteria to ensure accurate and detailed SIF measurements. Retrieving SIF both in the red and far-red wavelength range, as well as various vegetation indices at the same time, will help to study how vegetation phenology affects the SIF signal. The ratio of the two fluorescence peaks in the red and far-red wavelength range can be used for several applications, e.g., the determination of the chlorophyll content at leaf level (Gitelson and Merzlyak, 1997; Gitelson et al., 1999) or canopy structure. Changes in the fluorescence ratio also occur in response to environmental factors such as temperature (Agati et al., 2000) and light (Genty et al., 1990).

A major challenge of SIF measurements is to discern the small SIF signal (less than 3% in the far-red wavelength range) from the much larger background signal of the reflected sunlight. Spectral fitting routines permit SIF retrieval in multiple spectral bands, thus providing information on the shape of the fluorescence spectrum. Most published papers report on spectral fitting methods to extract SIF by exploiting either the oxygen absorption bands at 760 nm (O_2-A) or at 690 nm (O_2-B) (e.g., Meroni et al., 2009; Rascher et al., 2009, 2015; Rossini et al., 2015; Damm et al., 2015; Cogliati et al., 2015b, and references therein). Another approach to retrieve SIF is through the use of the in-filling of Fraunhofer line depth (e.g., Plascyk and Gabriel, 1975), which has been used for satellite SIF retrievals (Joiner et al., 2011, 2012b; Frankenberg et al., 2011b; Guanter et al., 2012; Joiner et al., 2013; Frankenberg et al., 2014; Köhler et al., 2015) as well as for some ground-based SIF measurements (e.g., Guanter et al., 2013). The Fraunhofer line approach has the advantage that it is less sensitive to atmospheric scattering which will be instrumental for evaluating SIF during partially cloudy conditions, thus overcoming the current limitation of clear sky conditions (e.g., Yang et al., 2017). However, the SIF retrieval based on in-filling of Fraunhofer lines requires an instrument with excellent thermal stability, high spectral resolution, and high signal-to-noise ratios (Guanter et al., 2013).

Another challenge when interpreting SIF is that of spatial inhomogeneities and averaging in the canopy. Several observations and modeling studies have shown that directional variations in SIF measurements exist (e.g., Liu et al., 2016, and references therein). There is thus a need to observe SIF from different viewing directions and different locations above the canopy. Spatially resolved SIF measurements will allow observation of different species in the canopy, and provide a wealth of information on the radiative transfer in the canopy, including the dependences of vegetation indices, such as PRI (Hilker et al., 2011), on the changes in the radiative transfer in the canopy. Simultaneous co-centered observations of red and far-red SIF, as well as vegetation indices with a small field of view, can improve the understanding of the influence on the SIF signal from stress, viewing geometry, or radiation environment.

In this manuscript a novel state-of-the-art spectrometer system - PhotoSpec - which includes the above-mentioned design criteria is presented. Section 2 develops a theoretical framework for SIF measurements. The instrumental set-up is described in Section 3 and the retrieval algorithm in Section 4. The capabilities of PhotoSpec are demonstrated with measurements of the diurnal cycle of the SIF signal of single broad leaves and grass, as well as dark-light transitions. Results of the first field measurements of this novel system in the rainforest of La Selva Biological Station in Costa Rica are reported in Section 5.

2. Theory

The detection of SIF is based on measuring the change of the optical densities of a well-known narrow spectral feature in the presence of a fluorescence signal, which acts as an additive offset (Fig. 1). Two types of spectral features are available in the fluorescence emission wavelength range: oxygen absorptions around 680 and 760 nm, and solar Fraunhofer lines, which originate in the sun's photosphere (Fraunhofer, 1817; Kirchhoff, 1860). If the absorption optical densities (I/I_0) are known, as in the case of Fraunhofer lines, a simple mathematical framework can be developed to illustrate the principle of SIF remote sensing. We consider a narrow Fraunhofer line with an optical density $-\ln(I/I_0)$, where I is the intensity in the band minimum and I_0 is the intensity of the band edges interpolated to the wavelength of the band minimum (Fig. 1). The intensity leaving the canopy outside and inside the line, I_0^C and I^C, can be written as:

$$I_0^C = a^C \cdot I_0 + I_{SIF}$$
$$I^C = a^C \cdot I + I_{SIF} \quad (1)$$

with a^C being the spectrally smooth reflectance of the canopy and I_{SIF} the fluorescence signal emitted by the canopy.

The change in optical density due to the additive emission by SIF can then be approximated as follows (see derivation of equation in the supplement Section S1.1):

$$\ln\left(\frac{I^C}{I_0^C}\right) \approx \ln\left(\frac{I}{I_0}\right)\cdot\left(1 - \frac{I_{SIF}}{a^C \cdot I_0}\right). \quad (2)$$

This equation states that the optical density of any spectral band is reduced by the ratio of the SIF radiance, I_{SIF}, and the canopy radiance $a^C \cdot I_0$. This fraction is typically in the range of 0–0.03 in the far-red and 0–0.3 in the red wavelength range, where a^C is small. For optically thin lines, any instrument must be able to accurately measure changes in optical density of much less than 1%. In addition, the optical density of the spectral features in the absence of a fluorescence signal, i.e., $\ln(I/I_0)$ must be known to better than 1–2‰.

2.1. Retrieval methods

Before describing the design of our new SIF instrument, it is useful to consider the theory of SIF measurements and retrievals, in particular with respect to instrumental properties that are common with spectrometer/detector systems (see Platt and Stutz, 2008 for details on the components typically used for atmospheric remote sensing). Meroni et al. (2009) and references therein summarize more recent SIF retrieval strategies with a particular focus on the oxygen absorption bands using observations from the ground, aircraft, and satellite. In contrast, our approach leverages retrieval techniques from the atmospheric science community with a focus on Fraunhofer lines and least-square retrieval techniques. These theoretical consideration will also be the basis of the PhotoSpec retrieval described in Section 4.

We begin with setting up a general equation of the spectrum recorded by a SIF spectrometer pointing at the canopy $I^C(\lambda)$ and at a non-fluorescent optical component, typically a diffuser, to measure a solar reference: $I^D(\lambda)$. SIF retrievals are based on the comparison of these two spectra. The intensity measured by a typical SIF instrument from the diffuser, $I^D(\lambda)$, and the canopy, $I^C(\lambda)$, can be written as follows:

$$I^D(\lambda) = T(\lambda)\cdot(a^D(\lambda)\cdot I(\lambda) + I_{stray}(\lambda)) + I_{DC} + I_{offset} \quad (3)$$

$$I^C(\lambda) = T(\lambda)\cdot(a^C(\lambda)\cdot I(\lambda) + I_{stray}(\lambda) + I_{SIF}(\lambda)) + I_{DC} + I_{offset}, \quad (4)$$

where $I(\lambda)$ is the incoming solar irradiance (for simplicity, we ignore the impact of solar angles and radiance-irradiance conversion here). $I_{stray}(\lambda)$ is stray light in the spectrometer from grating imperfections in combination with diffuse reflections in the spectrometer, which is often 0.1–1 % of the signal (Platt and Stutz, 2008). $a^D(\lambda)$ and $a^C(\lambda)$ are the reflectivities/transmissivities of the diffuser and the reflectivity of the canopy, respectively. $T(\lambda)$ is the instrument sensitivity. The signal typically also contains thermal detector dark current, I_{DC}, which depends on detector temperature as well as the signal level (see Platt and Stutz, 2008 for details). I_{offset} is the electronic zero signal that is imposed by the spectrometer electronics.

2.1.1. Linearized retrieval in an ideal case

In an ideal case, stray light is negligible, dark current and offset can be perfectly corrected, and the detector sensitivity cancels out when comparing the two spectra. Eqs. (3) and (4) can then be simplified to:

$$I^D(\lambda) = a^D(\lambda)\cdot I_0(\lambda)$$
$$I^C(\lambda) = a^C(\lambda)\cdot I_0(\lambda) + I_{SIF}(\lambda). \quad (5)$$

The linearization of the SIF retrieval based on $I^D(\lambda)$ and $I^C(\lambda)$ follows the general approach common for trace gas retrievals in solar spectra using a Taylor series of the natural logarithm of the intensities (see derivation of equation in the supplement in Section S1.2):

$$\ln(I^C(\lambda)) \approx \ln(I^D(\lambda)) + \ln\left(\frac{a^C(\lambda)}{a^D(\lambda)}\right) + \frac{I_{SIF}(\lambda)}{I^C(\lambda)}. \quad (6)$$

This linearization now permits the use of a linear least-square fitting method to analyze $\ln(I^C(\lambda))$ by fitting the following forward model function $f(\lambda)$:

$$f(\lambda) = \ln(I^D(\lambda)) + P_\alpha(\lambda) + C_{SIF}\frac{R_{SIF}(\lambda)}{I^C(\lambda)}. \quad (7)$$

Here, $P_\alpha(\lambda)$ is a polynomial of order α that is used to describe $\ln(a^C(\lambda)/a^D(\lambda))$, which both have a smooth spectral shape. $R_{SIF}(\lambda)$ is a reference spectrum for the SIF emission signal, prescribing the spectral shape of the SIF emission, which is scaled with the scalar fit factor for SIF, C_{SIF}.

As discussed in detail in the supplement in Section S1.2, the error of this linearization is $-\frac{1}{2}\left(\frac{I_{SIF}(\lambda)}{I^C(\lambda)}\right)^2$.

The linearization thus introduces a relative negative error(bias) on $\frac{I_{SIF}(\lambda)}{I^D(\lambda)}$ of 0–1.5 % in the far-red wavelength range and 0–15 % in the red wavelength range. While the error (bias) is small in the far-red, it can be considerable in the red wavelength range. One solution to overcome this challenge would be to perform a fully non-linear retrieval, as done for GOSAT and OCO-2 (Frankenberg et al., 2011a). However, linear retrievals have several advantages, including faster computing times and a guarantee of finding the mathematical optimal solution of the optimization. We therefore developed a simple two-step linear least-squares fitting method to overcome the approximation limitations in the linearization approach.

2.1.2. Two-step linearized retrieval method

The basic idea of this approach is to use a first step linear retrieval to determine an approximate solution of $I_{SIF}(\lambda)$. This $I_{SIF}{}^1(\lambda)$ is within ~ 10% of the true I_{SIF}. For the second step, $I_{SIF}{}^1(\lambda)$ is subtracted from $I^C(\lambda)$ to create $I^{C,1}(\lambda) = I^C(\lambda) - I_{SIF}{}^1(\lambda)$. $I^{C,1}(\lambda)$, which still contains a small fraction of the original SIF signal, is now analyzed again using the same linearized approach. Because the residual SIF signal in $I^{C,1}$ is now in the range of 0–3 % in the red and 0–0.3 % in the far-red, the linearization can now be applied with only a small bias due to the approximations. The result of this retrieval is $I_{SIF}{}^2(\lambda)$ with an error of $\Delta I_{SIF}{}^2$. The overall SIF signal is then $I_{SIF} = I_{SIF}{}^1 + I_{SIF}{}^2$ with a negative bias of 0–1.5 % in the red and 0–0.15 % in the far-red. The statistical error of the two step retrieval is $\Delta I_{SIF} = \Delta I_{SIF}{}^2$. The subtraction of $I_{SIF}{}^1$ in the first step does not introduce any statistical uncertainty in the overall retrieval, as any uncertainty in $I_{SIF}{}^1$ will be corrected in the second step.

In order to test whether this approach does in fact yield the desired results we performed a Monte-Carlo test where SIF signals with relative magnitudes of: 0.001, 0.005, 0.01, 0.05, 0.1, 0.2, and 0.3, were added to a spectrum in the red wavelength range. Random noise spectra were then added with relative noise standard deviations of: 10^{-5},10^{-4},10^{-3},$5\cdot10^{-3}$,10^{-2}, and $5\cdot10^{-2}$. A spectral analysis was then performed on 1000 noisy spectra for each relative SIF signal and each relative noise level combination in a small wavelength interval from 680 to 686 nm. The results show that the first step of the SIF retrieval technique does not retrieve the correct signal (here set to 1) and that the difference increases with the relative SIF signal, as expected from the approximation (Fig. 2a). The sum of the first and second step, however, is very close to the true value of 1 (Fig. 2a), thus overcoming the limitation imposed by the linearization of the retrieval. This iterative retrieval approach can be expanded to more iterations, but we found that two iterations are sufficient to reduce the bias far below the statistical retrieval error imposed by noise and instrument deficiencies.

We also compared the frequency distribution for the 1000 fit results of the spectra with a relative SIF signal of 0.05 and noise levels of 0.5% with the expected frequency distribution from the average error calculated by the second step of the retrieval (Fig. 2b). The agreement of

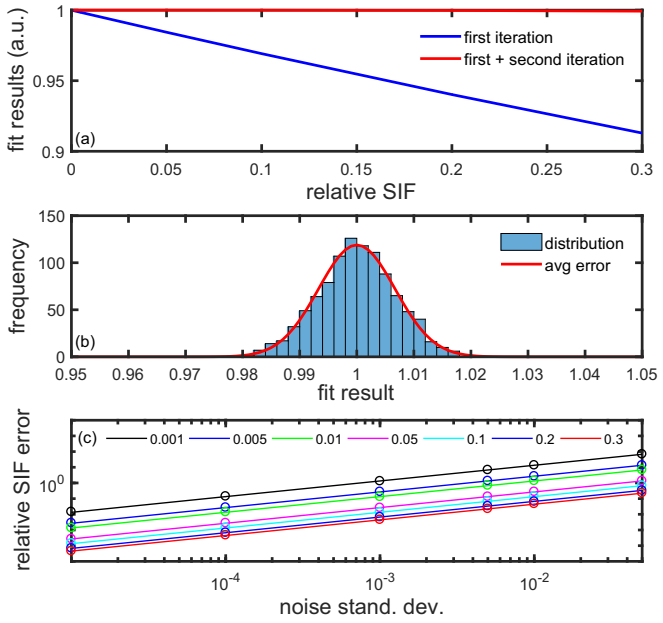

Fig. 2. Results of the Monte-Carlo tests of the new two-step SIF retrieval technique. Panel (a) shows the fit results of the first step and the sum of the first and second steps for an analysis in the red wavelength range. (b) The frequency distribution for fit results of 1000 spectra with a relative SIF signal of 0.05 and varying noise spectra of 0.5% standard deviation. The frequency distribution is compared to a Gaussian distribution with the width of the average error from the second step of the retrieval. Panel (c) shows the relative SIF error as a function of the noise and the relative SIF levels listed in the figure legend from the average fit error (line) and the standard deviation of the fit results in the Monte-Carlo test (circle).

this comparison confirms that the retrieval error of the second step does indeed represent the correct uncertainty of the fitting procedure. Fig. 2c compares the relative SIF error from the average fit error (line) with that derived using the standard deviation of the 1000 fit results for all combinations of relative SIF signal and noise level (circle). In all cases, there is strong agreement. Fig. 2c also illustrates how the retrieval can be improved with a reduction of noise.

2.2. Instrumental effects

2.2.1. Detector nonlinearity

Several commercial array detectors are known to have small detector nonlinearities in the range of ~1%. To understand the impact of the nonlinearity we will first investigate how the depth of an absorption band defined by I and I_0 changes for a given nonlinearity, and then apply these results to the theoretical SIF retrieval in Section 2.1.1.

We define the nonlinearity as a deviation from the proportionality between the incoming photon flux L and L_0, and the detector signal I and I_0, with L being the true photon flux entering the system and I being the measured intensity in the band minimum and L_0 and I_0 being the true photon flux and measured intensity of the band edges interpolated to the wavelength of the band minimum.

$$\begin{aligned} I_0 &= d_1 \cdot L_0 + d_2 \cdot L_0^2 \\ I &= d_1 \cdot L + d_2 \cdot L^2 \\ &= d_1 \cdot F \cdot L_0 + d_2 \cdot F^2 \cdot L_0^2 \qquad \text{where} \quad F = \frac{L}{L_0}. \end{aligned} \tag{8}$$

Here, the second quadratic term denotes the nonlinearity. Higher order terms are possible, but will be ignored here to keep the calculations simple. The treatment here should only be considered conceptually and it is best to entirely avoid or accurately correct nonlinearities as mentioned at the end of this section.

As derived in the supplement in Section S1.3, the optical density can be described as a function of F and the nonlinearity NL:

$$\ln\left(\frac{I}{I_0}\right) = \ln(F) - (1 - F) \cdot \mathrm{NL} \qquad \text{with} \qquad \mathrm{NL} = \frac{d_2}{d_1} \cdot L_0. \tag{9}$$

NL determines the deviation based on the linearity from the ratio of the quadratic and linear terms in Eq. (8) and depends on L_0. $\ln(F)$ is the optical density of the absorption line, and $(1 - F) \approx \ln(F)$ for a small F. The relative change of the optical density is thus directly proportional to NL.

This can now be compared to the general SIF linearization using F (derivation of equation in the supplement in Section S1.4):

$$\ln\left(\frac{I + I_{\mathrm{SIF}}}{I_0 + I_{\mathrm{SIF}}}\right) \approx \ln(F) - (1 - F) \cdot \frac{I_{\mathrm{SIF}}}{I_0}. \tag{10}$$

Comparing this to Eq. (9) shows that NL will influence the optical depth of the absorption line in exactly the same way as I_{SIF}/I_0. The error on the SIF signal due to a relative nonlinearity NL can be expressed as:

$$\Delta I_{\mathrm{SIF}} = I_0 \cdot \mathrm{NL}. \tag{11}$$

Considering that I_{SIF}/I_0 is typically in the range of 1–3 % in the far-red wavelength range, the requirements for the linearity of a detector are substantial. An uncorrected 0.1% nonlinearity over the saturation range of the detector can translate to an error of 3–10 % in the SIF signal. It is thus necessary to perform nonlinearity corrections or to find other means to avoid nonlinearity, for example by maintaining a constant detector signal level by varying the exposure time. Both of these methods are used for our PhotoSpec system. For airborne and spaceborne applications, maintaining a constant detector signal level is not feasible. Very accurate linearity measurements or the acquisition of reference targets over the entire detector dynamic range are thus required.

2.3. Dark current and offset correction

Typically, it is straightforward to correct the electronic offset by measuring the detector signal in the dark at the lowest possible exposure time. Changes in offset can be found when the detector electronics are exposed to varying temperatures, i.e., when SIF and offset measurements are performed at different temperatures. This can be avoided by thermally stabilizing the detector and its electronics. A few spectrometers have been found to heat up when many spectra are recorded rapidly after each other. This effect may also cause a change in offset and care has to be taken to avoid it.

The dark current of a typical array detector is highly temperature dependent, decreasing by a factor of two every ~5.5 K. The easiest way to avoid problems with the dark current correction is to cool the detector to the point when the dark signal is insignificant (less than 10^{-5} of the overall signal). If this cannot be achieved, the dark current can be corrected, but the nonlinearity of the dark signal with the saturation level of the detector needs to be considered. Platt and Stutz (2008) describe a method to correct for this effect.

Errors in correcting dark current and electronic offset lead to a direct absolute error in the SIF signal which can be positive or negative. This uncertainty should also be considered in the error calculation of the SIF measurements.

2.3.1. Stray light

A common challenge in a grating spectrometer system is the suppression of light originating from wavelengths other than those which are measured. Spectrometer stray light can originate from various sources, including incomplete wall absorption of higher or lower diffraction orders, imperfections in the optical elements of the spectrograph, dirt on optical elements, etc.

To investigate the effect of stray light on SIF retrievals we will use

the formalism and linearization introduced in Eq. (5), and expand it to include a stray light contribution. We can assume a constant stray light component I_{stray} across the narrow range of a Fraunhofer line. Analogous to Eq. (2), we can derive a linear approximation for the joint impact of I_{SIF} and I^C_{stray}:

$$\begin{aligned} I^C &= a^C \cdot I + I_{SIF} + I^C_{stray} \cdot \\ I^C_0 &= a^C \cdot I_0 + I_{SIF} + I^C_{stray} \\ \ln\left(\frac{I^C}{I^C_0}\right) &\approx \ln\left(\frac{I}{I_0}\right) \cdot \left(1 - \frac{I^C_{stray}}{a^C \cdot I_0} - \frac{I_{SIF}}{a^C \cdot I_0}\right). \end{aligned} \tag{12}$$

This equation shows that stray light in the spectrometer could have a considerable impact on the retrieval of a SIF signal as it affects the optical depths in exactly the same way as SIF. In the best case scenario, however, the stray light component in the reference target (diffuser) and the canopy spectrum will be identical and thus cancel out (unlike SIF). However, the situation in practical applications is more complex, as a diffuser measurement might exhibit a different amount of stray light. Using the same formalism as above, the diffuser measurement can be written as follows:

$$\begin{aligned} I^D &= a^D \cdot I + I^D_{stray} \\ I^D_0 &= a^D \cdot I_0 + I^D_{stray} \\ \ln\left(\frac{I^D}{I^D_0}\right) &\approx \ln\left(\frac{I}{I_0}\right) \cdot \left(1 - \frac{I^D_{stray}}{a^D \cdot I_0}\right). \end{aligned} \tag{13}$$

In a typical SIF retrieval $\ln\left(\frac{I^D}{I^D_0}\right)$ is used as $\ln\left(\frac{I}{I_0}\right)$ in Eq. (12), and for a constant stray light component in both observations the stray light effect would cancel out. Unfortunately, the origin of stray light makes it highly unlikely that $\frac{I^C_{stray}}{I_0}$ is identical to $\frac{I^D_{stray}}{I_0}$, and the relative SIF error introduced by stray light on the retrieved $\ln\left(\frac{I_{SIF}}{I_0}\right)$ is thus:

$$\Delta I^{rel}_{SIF,stray} = \frac{I^D_{stray}}{a^D \cdot I_0} - \frac{I^C_{stray}}{a^C \cdot I_0}. \tag{14}$$

Spectrometer stray light is difficult to measure as every wavelength of incoming light, λ_{in}, will uniquely contribute to the signal at the observed wavelength λ. A general description of stray light as a function of the incoming intensity $I_{in}(\lambda_{in})$ is:

$$\begin{aligned} I_{stray}(\lambda) &= \sum \delta(\lambda, \lambda_{in}) \cdot I_{in}(\lambda_{in}) \\ &= I_{tot} \cdot \sum \delta(\lambda, \lambda_{in}) \cdot f(\lambda_{in}) \qquad \text{where} \quad I_{in}(\lambda_{in}) = I_{tot} \cdot f(\lambda_{in}). \end{aligned} \tag{15}$$

The function $\delta(\lambda,\lambda_{in})$ is typically unknown as it requires specialized equipment and considerable effort to determine it for each spectrometer. However, we can make some simplified calculations to determine a typical stray light error in a SIF retrieval. We use observations of a basil leaf and a ground glass diffuser made by the same grating spectrometer to provide the spectral characteristics of the incoming radiance in both cases. Typical stray light information from the manufacturers, as well as from our previous experience, puts the relative stray light at $\frac{I^D_{stray}}{a^D I_0} \approx 0.005$ at 682 and 745 nm (Platt and Stutz, 2008). We assume that all wavelengths of the incoming radiance contribute equally to this stray light. This then leads to $\delta(\lambda,\lambda_{in}) \approx 1.8 \cdot 10^{-5}$. We will then use this δ for our hypothetical instrument, thus calculating I_{stray} for the diffuser and canopy case for an instrument measuring in the red and far-red SIF wavelength range. The first case we analyze is that of an instrument measuring SIF without any additional measure to reduce stray light. In this case we estimate $\frac{I^D_{stray}}{I^D_0} \approx 5{\cdot}10^{-3}$ and $\frac{I^C_{stray}}{I^C_0} \approx 8{\cdot}10^{-4}$ and the error on the relative SIF signal becomes $\Delta I_{SIF,stray}{}^{rel} \approx -0.0042$. Comparing this to a typical relative SIF signal of $\frac{I_{SIF}}{I_0} \approx 0.01$ yields a 42% error on a SIF retrieval. The cause of this large error is the change of the spectrum shape due to the leaf absorptions by chlorophyll-a, i.e., the relative stray light contribution at 745 nm is reduced in the canopy case due to the relative lower radiances in the visible wavelength range compared to those from the diffuser.

This is not a statistical error, but rather a bias that will be present with or without a SIF signal. The same calculation can be done for 682 nm, i.e., in the red wavelength range. Here $\Delta I_{SIF,stray}{}^{rel} \approx -0.0037$. However, because $\frac{I_{SIF}}{I_0} \approx 0.1$ at this wavelength, the stray light error only contributes 3.7%. The reason for this lower error is the higher relative SIF signal due to the much lower canopy reflectance. Both calculations show that stray light can introduce a considerable uncertainty in SIF observations, if no additional measures are taken. Luckily, most SIF instruments, including the one we will present in the next section, use high-pass glass filters that cut out light below 590 nm in the red or 695 nm in the far-red. Repeating our calculations including these filters result in much lower stray light contributions of $\Delta I_{SIF,stray}{}^{rel} \approx -0.0026$ or 2.5% at 682 nm and $\Delta I_{SIF,stray}{}^{rel} \approx -10^{-4}$ or 1% at 745 nm. With these filters, stray light introduces only a small bias into the SIF observations as long as stray light is in the range of $\sim$ 0.5%. It is thus clear that SIF instruments should be equipped with long-pass filters that eliminate as much of the unneeded lower wavelengths as possible.

3. The PhotoSpec system

The theoretical consideration in the previous section led us to develop a novel ground-based spectrometer system - PhotoSpec - to perform spatially resolved simultaneous red/far-red SIF and vegetation index observations as well as measurements of reflectance. In order to observe SIF using Fraunhofer band in-filling and address the associated challenges, the instrumental set-up and retrieval technique are based on extensive experience with Differential Optical Absorption Spectroscopy (DOAS) (Platt and Stutz, 2008). DOAS is a remote sensing technique that has been used for decades to measure small atmospheric trace gas absorptions. The need to measure optical density changes down to 10^{-4} makes the instrument requirements and the retrieval for DOAS similar to those required for SIF. PhotoSpec was thus designed for high instrument stability, small stray light, small detector nonlinearity, and low noise.

Fig. 3 shows a schematic drawing of the PhotoSpec design. A two-dimensional(2D) scanning telescope unit is used to collect reflected sunlight and SIF from any location in the canopy. Direct sunlight can be measured by turning the scanner onto the bottom of an upward-looking diffuser. The scanner/telescope feeds light into a long single fiber which is connected to a fiber bundle. This tri-furcated bundle distributes the observed light to three thermally stabilized commercial spectrometers. A rugged industrial computer is used for data acquisition to control the scanner, spectrometers, and temperatures, and to record PAR data. The PhotoSpec instrument is designed to operate fully automatically with near real-time SIF retrievals and can be controlled remotely. The following sections will describe each of these components in more detail.

3.1. The 2D scanning telescope unit

The 2D scanning telescope unit consists of two parts that can be rotated by high precision servo motors (Fig. 3): A rotating prism scans in elevation direction from zenith to nadir. This prism is mounted in a channel that rotates in the azimuth direction about the telescope vertical axis. The azimuth channel can rotate 360°. The optical path through the telescope starts with sunlight entering through the first rotating elevation prism (12.5 mm uncoated N-BK7 total internal reflection prism), reflects the light to a secondary, identical prism mounted at the telescope vertical axis. This prism reflects the light into the telescope, which consists of an uncoated, plano-convex lens (diameter d = 12.7 mm, focal length f = 49.15 mm) that focuses the light onto a single glass fiber of 0.6 mm diameter. The telescope is focused to infinity and thus has a field of view (FOV) of 0.7°(full angle). The

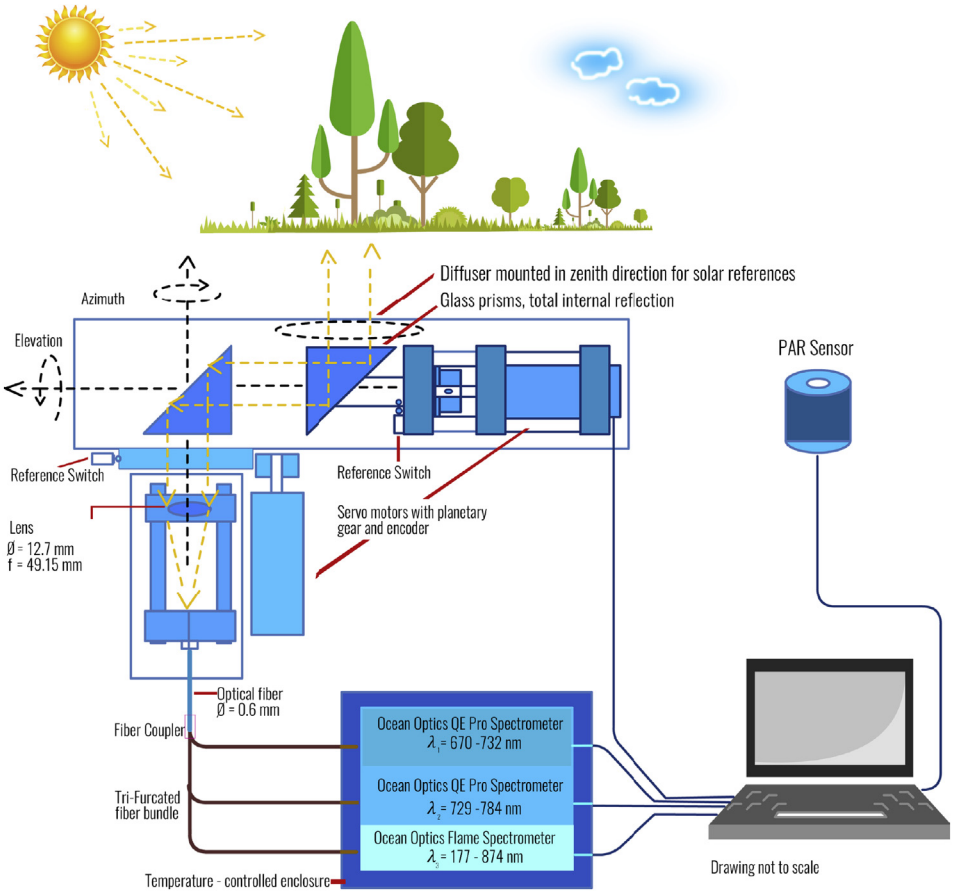

Fig. 3. Schematic layout of the PhotoSpec system.

advantage of this optical set-up is that the scanner/telescope throughput is independent of the pointing direction, as all optical elements are passed through the same angle for all viewing directions.

The scanner unit collects light at user selectable azimuth and elevation angles using two small servo motors with planetary gears and a Hall encoder (Faulhaber 1266 S O12 B K1855). The elevation and azimuth scanning unit each include a limit switch, which serves as an absolute angle reference. Laboratory tests show that we can determine the angular position of each motor to better than 0.1°.

Depending on the needs in the field, the single fiber has a length of 5–100 m and is connected to a tri-furcated distributor fiber bundle (length $l = 2$ m) via a fiber coupler. The distributor bundle has a single circular end on one side and splits into three ends with 15 fibers each (0.06 mm diameter) on the other side. The 15 single optical fibers are arranged linearly in a column and serve as the entrance slit of the three spectrometers, with a height of 0.9 mm and a width of 0.06 mm. This fiber arrangement ensures that all three spectrometers simultaneously observe the same target in the canopy.

A diffuser plate (ground glass or Teflon coated glass) is mounted on top of the elevation channel (zenith direction) to allow regular measurements of solar reference spectra (diffuser spectra). In order to allow regular measurements of the spectrometer dark current and offset, a black target is located inside the back of the elevation channel, which is only used at night.

The 2D scanning telescope unit has a size of approximately ($33 \times 11 \times 42$) cm and can be mounted on observation towers above a canopy. The narrow field of view of 0.7° (12.2 mrad) yields an observed footprint of the 2D scanning telescope unit ($x = 2h \tan(\mathrm{FOV}/2)$) of approximately 12 cm diameter from a height above the canopy of $h = 10$ m and approximately 50 cm diameter for $h = 40$ m. This footprint is sufficient to target single trees individually, gaps in canopies, or sunlit and shaded areas over the entire canopy.

3.2. The spectrometer system

The linear ends of the tri-furcated fiber bundle serve as entrance slits for three thermally-stabilized commercial spectrometers from Ocean Optics, Inc., Florida, USA (two QEPro spectrometers, one UV-vis Flame spectrometer, Table 1). The two QEPro spectrometers

Table 1
Spectral characteristics of the Ocean Optics spectrometer in the PhotoSpec instrument.

	Red	Far-red	UV/vis
Spectrometer	QEPro 1	QEPro 2	Flame
Wavelength [nm]	670–732[1]	729–784	177–874
Number of detector pixels	1044	1044	2048
Dispersion [nm/pixel]	0.074	0.067	0.382
FWHM [nm]	0.3	0.3	1.2
Grating [grooves/mm]	2400	2400	600
f/#	f/4	f/4	f/2
Filter	OG590	RG695	2. order
Entrance slit [μm]	none	none	25
Detector	Hamamatsu S7031-1006	Hamamatsu S7031-1006	Sony ILX511B linear silicon CCD array
Quantum efficiency (peak) [%]	90	90	90

[1] 670–732 nm in early PhotoSpec version, 650–712 nm in final PhotoSpec version.

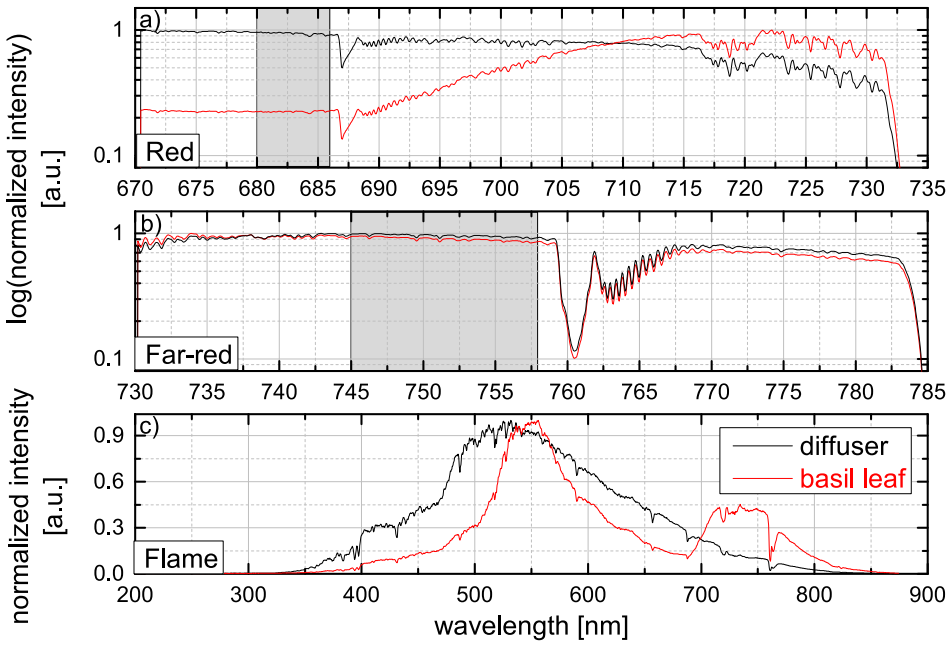

Fig. 4. PhotoSpec spectra of a diffuser plate (black line) and a basil leaf (red line) acquired on the UCLA Math Sciences roof on 10/26/2016. Panels a) and b) show high resolution spectra for SIF Fraunhofer line based retrievals. The gray box marks the wavelength range used for the SIF spectral retrieval. Panel c) shows broad-band measurements for vegetation indices, PRI, and chlorophyll content determination.

(henceforth referred to as ‘ red’ and ‘ far-red’) cover a SIF retrieval wavelength range at high spectral resolution (red: λ = 670–732 nm (prototype) λ = 650–712 nm (final version), FWHM = 0.3 nm; Far-red: λ = 729–784 nm, FWHM = 0.3 nm), which encompass the two fluorescence emission peaks around 685 and 740 nm. The PhotoSpec FWHM of 0.3 nm is determined by the fiber width of 0.06 mm, which acts as an entrance slit. The Flame spectrometer of the PhotoSpec prototype provides moderate resolution spectra (λ = 177–874 nm, 1.2 nm FWHM) in order to retrieve vegetation indices (Fig. 4). The UV/vis Flame spectrometer was exchanged by a vis-NIR Flame, with a more suitable wavelength range for the calculation of vegetation indices (λ = 339–1022 nm) in all later versions of the PhotoSpec instrument.

The arrangement of the optical bench of the spectrometers is based on the crossed Czerny-Turner principle and the spectrum is measured by a CCD detector. The QEPro spectrometers are equipped with a 2400 groove/mm grating and a back-thinned Hamamatsu S7031-1006 detector with 1044 pixels, whereas the Flame spectrometer has a 600 groove/mm grating and a Sony ILX511B linear silicon CCD array with 2048 pixels. The detectors in the QEPro spectrometers are typically kept at − 10°C to reduce dark current. The red and far-red QEPro spectrometers are equipped with an OG590 and a RG695 optical longpass filters, respectively, and the Flame spectrometer with a 25 μm entrance slit and an order sorting filter at the detector. Table 1 summarizes the characteristics of the three spectrometers in the PhotoSpec instrument. It should be noted that the filter in the far-red spectrometer of the prototype instrument cuts out light below 590 nm, not 695 nm. The filter will be replaced by the correct filter in future deployments of the prototype instrument and all newly-built PhotoSpec instruments have the correct filter installed. The error in the far-red SIF signal due to stray light will thus be larger for the data shown in this study than for future data sets. Assuming a relative SIF signal of $\frac{I_{SIF}}{I_0} \approx 0.01$, the stray light error in the far-red SIF signal due to the incorrect filter adds up to 11%.

In order to ensure that the spectrometers are optically stable, i.e., do not show changes in their spectroscopic or electronic dark current and linearity (Section 2.2.1 and 2.3) performance, we use a two-stage temperature stabilization design. The three spectrometers are mounted inside a thermally-stabilized enclosure. The air inside of the enclosure is cooled to 18°C using a Peltier cooler (TE Technology Peltier module + TC-48-20 controller) with a temperature stability of approximately ± 0.1 K for the spectrometer environment, while slightly heating the spectrometers to 25°C with a temperature stability of better than ± 0.05 K (Omega Polyimide Film insulated flexible heaters and a 585-05-12 TECPak thermal controller from Arroyo Instruments).

3.3. PAR sensor

The telescope unit also includes a commercial Photosynthetic Active Radiation (PAR) sensor (LICOR LI-190R) to have an independent measurement of direct/diffuse light. This PAR signal can also be used as a calibration of the PhotoSpec when comparing the PAR signal of the LICOR sensor to the PAR signal retrieved using the Flame spectrometer. The PAR sensor is read out with a special purpose amplifier (UTA amplifier, EME Systems) combined with an Ethernet-based high-speed multifunction data acquisition board (Measurement Computing E-1608), both of which are mounted inside the telescope housing. The PAR sensor is operated at a time resolution of 1 s to provide high frequency information on the radiative properties of the atmosphere. The PAR data is recorded by the main instrument computer. The LI-190R sensor was calibrated at the factory against a standardized lamp, which itself was calibrated against a National Institute of Standards and Technology (NIST) lamp. The uncertainty of the calibration is ± 5%, traceable to the NIST standards. The LICOR sensor calibration multiplier used in this study is $c_{LICOR} = 140.39\ \mu mol\ s^{-1}m^{-2}\mu A^{-1}$, and the UTA amplifier gain factor $g_{UTA} = 0.3\ V/\mu A$. The PAR signal is given in units of $\mu mol\ s^{-1}m^{-2}$.

3.4. Data acquisition and measurement sequences

A rugged industrial computer (LOGISYS LG-P675E) is used for data acquisition, to control the motors and the temperature in the spectrometer box, and to record the PAR data. The control software for the scanner/telescope and the spectrometers is based on DOASIS (Kraus, 2006), which was developed by the University of Heidelberg for remote sensing DOAS instruments.

A typical observation sequence in the field starts with the measurement of a diffuser spectrum, followed by a list of different azimuth and elevation angle combinations pointing towards different vegetation targets with a time resolution of approximately 20–60 s per target. Spectra of the same target are recorded simultaneously with all three spectrometers during the same time interval. Different scanning strategies can be applied, e.g., 1) a target sequence with a list of specific

targets which are scanned consecutively, or 2) to create ' chess-pattern' rasters over one single species, or 3) elevation scans across the canopy with a fixed azimuth angle. Since the spectrometers have a slight detector nonlinearity in the recorded intensities, which can result in residual structures in the spectral retrieval (Section 2.2.1), the saturation level is set to a fixed level through an automatic adjustment of the integration time and number of scans. For the far-red intensities, the saturation level is set to 50%, i.e., the number of counts per spectrum should be around 50% of the maximum number of counts (maximum: 200,000 counts for the red and far-red spectrometer, 65,535 counts for the Flame spectrometer). Due to the strong absorption of the canopy in the red wavelength range (Fig. 4), the saturation level in the red SIF analysis range is set to 10%, so that the right portion of the red spectrum at higher wavelengths is not saturated. The detector nonlinearity in the recorded intensities will still be corrected prior to the SIF retrieval on a pixel by pixel basis for each spectrometer. The scanning strategies are continuously repeated as long as the solar zenith angle (SZA) is lower than 90°. Once a day during nighttime (SZA > 100°), detector dark current and offset measurements are performed.

3.4.1. Calibration of telescope viewing direction

In order to take advantage of the ability of the 2D scanning telescope unit to point at specific targets, it is necessary to calibrate the PhotoSpec viewing direction after final installation in the field. We developed a method that allows us to accurately aim the PhotoSpec in a canopy: Different vegetation targets within the FOV of the telescope are selected during the day, often supported by photographs of the canopy. At night, the light from a strong light source, e.g. a Xenon lamp (Hamamatsu L2274, 150 W) or a white LED, is fed into the fiber coupler end of the extension fiber to go backwards through the telescope. Thus, the view of the telescope is projected by the light beam into the canopy. The azimuth and elevation angle of the different targets are then determined by moving the 2D scanning telescope unit until the light beam is pointing onto the chosen targets. Tests showed that the accuracy of the scanner and this calibration approach is better than 0.1°. Because the plant structure changes with time and the leaves are also moving in the wind, raster scans over one single species are often performed with a step size as small as the FOV to identify variations due to changes in the phenological phase of plants or leaf movement.

3.5. Radiometric calibration

The optical set-up and the typically complex field installation require that the radiometric calibration of PhotoSpec is performed in the field, often on top of a tower above the canopy. The calibration is determined for each spectrometer, i, and each wavelength, λ, by relating a measured signal $S_i(\lambda)$ (units: counts/ s) to the irradiance $I_i(\lambda)$ with a calibration factor $c_{cal_i}(\lambda)$:

$$I_i(\lambda) = c_{cal_i}(\lambda) \cdot S_i(\lambda) \quad (16)$$

In order to determine $c_{cal_i}(\lambda)$ in the field, a calibrated diffuse reflectance standard (Spectralon SRM-99, LabSphere Inc., NH, USA) is mounted below and somewhat in front of the telescope/scanner assembly. This reflectance standard is highly Lambertian, and has a reflectivity of 99% over a wavelength range from 250 to 2500 nm (https://www.labsphere.com). The telescope is pointed onto the reflectance standard and measurements of reflected sunlight are performed continuously with integration times of 20–60 s.

We used two radiometric calibration approaches to determine $I(\lambda)$ during the development of PhotoSpec. A preliminary calibration, which used theoretical calculations for direct solar irradiance on a clear day, was found to be less ideal as it requires the simultaneous measurement of aerosol optical thickness (AOT) and is not suitable for cloudy conditions. The final calibration approach uses parallel irradiance measurements using a calibrated spectrometer from Ocean Optics. Because this method was not yet available for some of the measurements presented in the rest of this manuscript, both calibration methods will be discussed in the following sections.

3.5.1. Preliminary radiometric calibration

For the preliminary calibration, spectra of sunlight reflected by the reflectance standard are recorded on selected cloud-free days. The calibration factor of Eq. (16) can then be calculated according to:

$$c_{cal_i}(\lambda) = \frac{I_{solar_i}(\lambda) \cdot \cos(SZA) \cdot e^{(-(\tau_{Rayleigh} + \tau_{aerosol})/cos(SZA))}}{S_i(\lambda)}, \quad (17)$$

with the numerator being the solar irradiance on the reflectance standard and $S_i(\lambda)$ the measured signal of each spectrometer i, respectively. $I_{solar_i}(\lambda)$ is derived from a high-resolution solar irradiance spectrum (Kurucz et al., 1984; Chance and Kurucz, 2010), which is convoluted with measured and normalized mercury or argon reference emission lines, to adapt to the spectral resolution of the respective spectrometer. The average Kurucz solar irradiance for the red (λ = 680–686 nm) and far-red (λ = 745–758 nm) SIF analysis wavelength range is 0.238 and 0.204 W sr^{-1} m^{-2} nm^{-1}, respectively. The other terms in the nominator are the geometric correction, cos(SZA), due to the sun's position, and corrections due to Rayleigh and aerosol scattering in the atmosphere. The Rayleigh scattering optical depth, $\tau_{Rayleigh}$, was determined using data from Bodhaine et al. (1999). AOT, $\tau_{aerosol}$, for the specific time and day of each measurement was determined from the closest available Aeronet station observations (https://aeronet.gsfc.nasa.gov; Santa Monica College: 34.01685°N, 118.47113°W).

The calibration measurements were performed over a two to four hour period around noon. To compute an average measured signal, we determined the average of $S_i(\lambda)/\cos(SZA)$. The red and far-red Spectralon signal $S_i(\lambda)/\cos(SZA)$ results in 6.6 and 4.7 · 10^5 counts/ s, respectively. The final preliminary calibration factor c_{cal} is then 0.36 and 0.43 μW s m^{-2} nm^{-1} sr^{-1} $counts^{-1}$ for the red and far-red SIF signal, respectively.

This preliminary radiometric calibration is applied to all measurements performed in Los Angeles. The systematic uncertainty of this preliminary calibration in Los Angeles is approximately 10% in the red and 15% in the far-red.

3.5.2. Radiometric calibration with calibration unit

Because the preliminary calibration method is not very precise and does not work in the presence of clouds, it was only used for the initial test data recorded at UCLA. For all further deployments, a radiometric calibration based on parallel solar irradiance observations was used. These parallel observations were performed with an Ocean Optics Flame spectrometer connected to a cosine corrector with a glass fiber. The cosine corrector is a Spectralon diffusing material. The Flame/cosine corrector unit is radiometrically calibrated in the field using a calibrated light source (Ocean Optics HL-3P-CAL).

For the PhotoSpec calibration, spectra of the calibrated Flame spectrometer are recorded with the cosine corrector pointing towards the zenith. The cosine corrector is mounted parallel to the ground. The PhotoSpec telescope unit, pointing onto the calibrated diffuse reflectance standard plate, makes simultaneous measurements. The calibration factor can then simply be determined from these observations using Eq. (16) and the dispersion of the respective spectrometers (see Section S2 in supplement for more information on the radiometric calibration). The average calibration factor c_{cal} for the red (λ = 680–686 nm) and far-red (λ = 745–758 nm) SIF analysis wavelength range is 1.2671 and 1.5922 μW s m^{-2} nm^{-1} sr^{-1} $counts^{-1}$, respectively. The calibration factor using the calibration unit is about a factor of three larger than the preliminary calibration factor due to the different measurement set-up of the first prototype version of the PhotoSpec instrument compared to the final instrument version, including different fiber lengths, different spectrometer temperatures, different optical alignments, etc. The calibration unit is used for the calibration

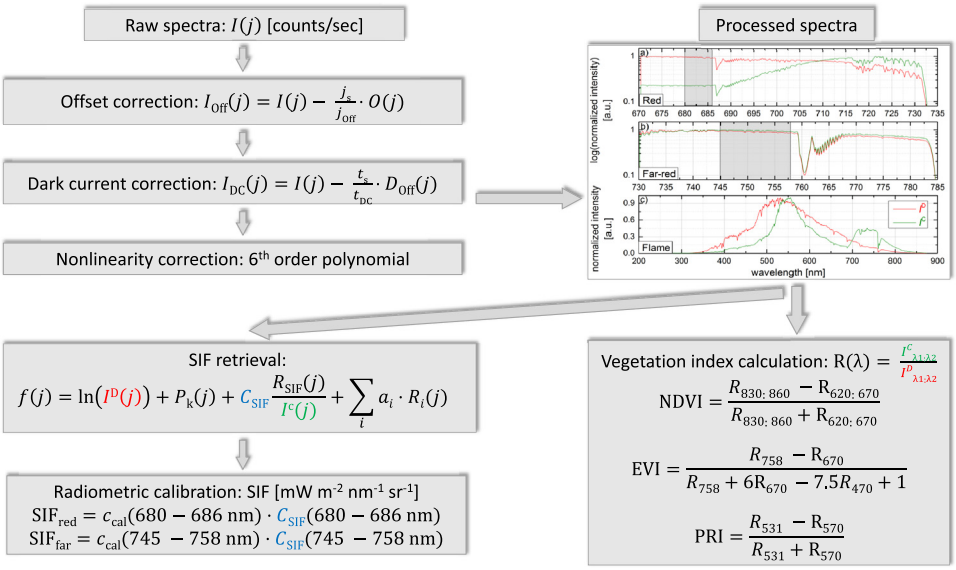

Fig. 5. Flow chart describing the processing chain of the PhotoSpec retrieval.

of the data collected at La Selva Biological Station in Costa Rica as well as for all further deployments of the PhotoSpec instrument. The main error of the radiometric calibration is given by the uncertainty of the calibration unit, which is quoted by the manufacturer as 5–7 % between 400 and 800 nm.

4. Data analysis

The spectra recorded by the PhotoSpec system permit the retrieval of SIF in different wavelength regions as well as the calculations of various vegetation indices. In this section we will describe the basic procedure to retrieve these parameters as currently implemented in the real-time and off-line analysis of the PhotoSpec. Fig. 5 summarizes the processing chain of the PhotoSpec retrieval which is described in the following.

4.1. Preprocessing of spectra

Prior to SIF retrieval and the calculation of the vegetation indices, each measured spectrum is corrected for electronic offset and dark current (Platt and Stutz, 2008). The electronic offset is a baseline signal that is common to all spectrometers and can be quantified by taking dark measurements at the shortest integration time (10 ms for the QEPro spectrometers and 3 ms for the Flame spectrometer of the PhotoSpec instrument), adding 100–10,000 spectra to reduce the noise in the electronic offset. However, certain spectrometers undergo a temperature change when the detector is read out at a high frequency. In the case of the PhotoSpec, no such effect was found in any of the spectrometers. Electronic offset spectra are recorded every night, and subtracted after scaling with the added scan number of each spectrum. Electronic offsets collected over a three month period in the field were found to linearly drift by approximately 10 counts/scan, with day to day variations of less than one count. Considering a typical signal level of 10^5 counts/scan for the QEPro spectrometers and the use of daily offset spectra, this results in a SIF error of $\sim 10^{-5}$. The offset error is somewhat larger for the Flame spectrometer, with a continuous drift of about 20 counts/scan over three months and a day to day variation of less than 5 counts/scan. This leads to an offset error of $1.7 \cdot 10^{-4}$ considering a typical signal of 30,000 counts/scan.

Dark current (DC) is caused by thermal recombination in the detector pixel and is highly temperature dependent (Platt and Stutz, 2008). Thus, the detectors have to be thermally stabilized at a constant low temperature to reduce the dark current and allow the accurate correction of the small residual dark current. The temperature of the PhotoSpec QEPro detectors is typically set between 0 and − 10°C, which leads to small DC's of 18 and 9 counts/ s, respectively. The Flame DC is somewhat higher, with 29 counts/ s, as the detector is not actively cooled. A DC spectrum with an integration time of 180 s and one scan is recorded every night for all PhotoSpec spectrometers. These spectra, after correcting the electronic offset, are then scaled to the total integration time of each daytime spectrum and subtracted. Because of the temperature stabilization of the PhotoSpec spectrometers, the DC is very constant over time, with long-term drifts over a three month period below 0.2%, which can be corrected by using daily DC spectra. Day to day variations in the DC are in the range of 0.6 counts/s for the QEPro's and 2.5 counts/s for the Flame spectrometer, thus resulting in relative errors of the typical QEPro signal of $6 \cdot 10^{-6}$ assuming a 30 s integration time and a signal of 10^5. The relative Flame error is $8 \cdot 10^{-5}$ for a 30 s integration time and a signal of 30,000 counts.

Detector nonlinearities can introduce significant errors in SIF retrievals (Section 2.2.1). While the PhotoSpec is designed to overcome this problem by adjusting the integration time to maintain the detector signal at a fixed level in the SIF retrieval windows (see Section 3.4), there are situations in which this approach is insufficient. It is thus advantageous to perform a linearity correction before the retrievals. The nonlinearity of all PhotoSpec spectrometers was measured in the laboratory using a halogen lamp with constant output by varying the integration time. Fig. 6 shows the nonlinearity curves for the PhotoSpec instrument. The nonlinearity of the two QEPro spectrometers is in the range of ~ 1% over the lower 90% of the detector saturation range. It reaches a maximum of 3–5 % in the upper 10% of the detector saturation range, which we have therefore excluded from any observations. The broadband spectrometer has a nonlinearity of ~10–15 % over a well-defined usable dynamic range. This nonlinearity compares well with those quoted by the manufacturer, but is statistically better constrained.

The nonlinearity is corrected on a pixel by pixel basis for each spectrometer with the 50% saturation correction factor set to 1 for all spectrometers using a fitted 6th -order polynomial. The residual nonlinearity after this correction has been determined through a linear fit to the corrected intensity to be about 10^{-5}% for the QEPro spectrometers and 0.01% for the Flame spectrometer.

Each spectrum has to be calibrated in wavelength, since the wavelength-pixel-mapping provided by the spectrometer manufacturer

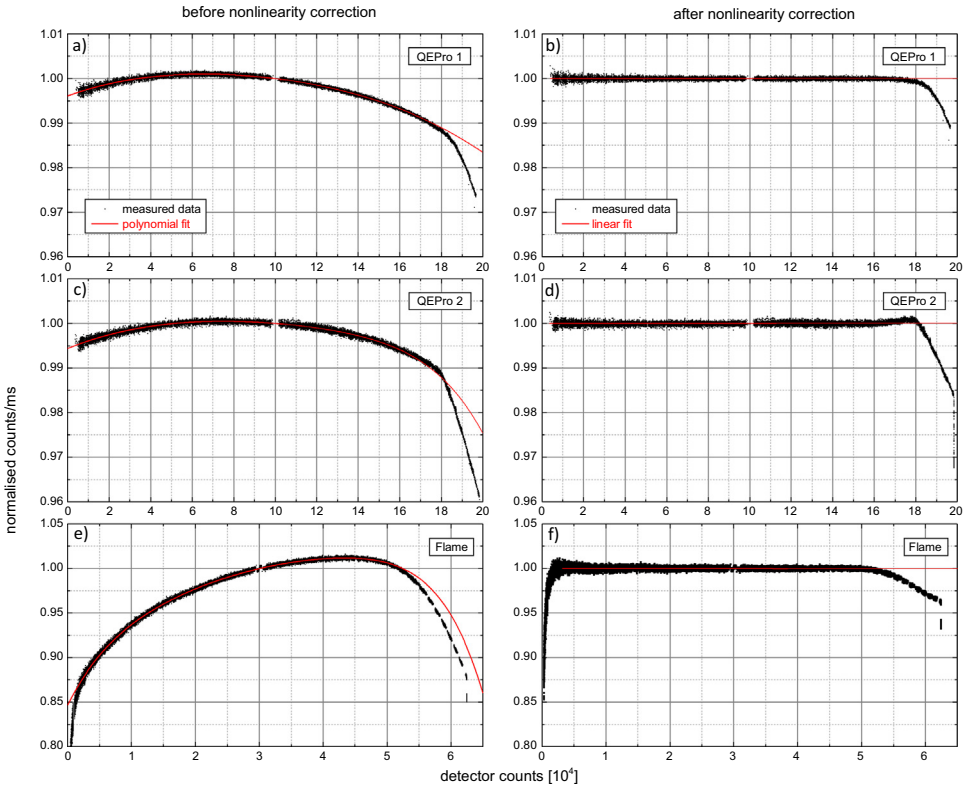

Fig. 6. Determination of the nonlinearity of the PhotoSpec spectrometers. Left panels: Measured counts per millisecond normalized to a reference value at an intensity level of 100,000 counts (panel a): QEPro 1 and panel c): QEPro 2) and of 30,000 counts (panel e): Flame). Right panels (b,d,f): Linearity curve after the correction by a 6th-order polynomial. The nonlinearity is corrected on a pixel by pixel basis for each spectrometer.

might have been performed at a different ambient temperature than the temperature used during the SIF measurements. Different ambient temperatures can cause shifts in the wavelength. The wavelength-pixel-mapping and the instrument function of the spectrometers are determined using mercury (Hg) and argon (Ar) spectra with known atomic emission lines position and width. The wavelength-pixel-mapping is also confirmed using the Fraunhofer lines in the solar diffuser reference spectra. The spectral shift of the spectrometers over a three month period was below 0.5 pixel (0.04 nm) for the red and 0.3 pixel (0.02 nm) for the far-red. This very small drift can be corrected during the SIF retrieval. The drift of the Flame spectrometer was insignificant for the vegetation index calculations.

4.2. SIF retrieval

The retrieval of the PhotoSpec red and far-red SIF signal uses the two step linearized approach described in Section 2.1.1. The retrieval algorithm for each step is based on our long experience with the DOAS method, which is summarized in Platt and Stutz (2008). The SIF retrieval uses the fact that the optical depth of Fraunhofer lines are determined in the sun's photosphere and that they remain unchanged in direct sunlight passing through the atmosphere. Any changes in the observed Fraunhofer line optical depth between the diffuser and the canopy are thus caused by the addition of the plant fluorescence signal. This idea has already been used for SIF retrievals from satellites (Joiner et al., 2011, 2012b; Frankenberg et al., 2011b; Wolanin et al., 2015).

The PhotoSpec retrieval steps are performed by fitting a model function, $f(j)$ to the logarithm of a canopy spectrum $\ln(I^C(j))$ using a combination of a linear and nonlinear least squares fit as described in Stutz and Platt (1996). In short, the fit uses the linear part to find the fit-parameters in the model function to minimize $\chi^2 = \sum_{j=1}^{n} (\ln(I^C(j)) - f(j))^2$, while the non-linear part is used to correct for small spectral shifts and squeezes. Here j corresponds to a specific spectrometer/detector channel and n to the total number of channels in the chosen wavelength interval. The model function $f(j)$ (Eq. (18)) is set up to provide an accurate description of the canopy spectrum:

$$f(j) = \ln(I^D(j)) + P_k(j) + C_{SIF}\frac{R_{SIF}(j)}{I^C(j)} + \sum a_i \cdot R_i(j). \quad (18)$$

This function is similar to Eq. (7), except that j is used instead of λ to reflect the fact that there is a limited number of n discrete data points. $\ln(I^D(j))$ is the logarithm of a temporally close, i.e., within 5–10 min, solar spectrum measured using the PhotoSpec diffuser. This spectrum provides the reference for the Fraunhofer bands in the retrieval. In the SIF retrieval, one diffuser spectrum is used as a solar spectrum for all following targets until the next diffuser spectrum is recorded. Because our retrieval is not sensitive to the fast changes in solar irradiance, i.e., we use the depth of Fraunhofer lines which are not impacted by clouds or other radiative transfer effects, we found that a 5–10 min interval to measure the diffuser is sufficient. $P_k(j)$ is a polynomial of degree k that is fitted to describe broadband spectral features. The SIF reference spectrum, $R_{SIF}(j)$, is based on a mean spectrum of samples spanning eight different species measured using an instrument described in Magney et al. (2017). $\frac{R_{SIF}(j)}{I^C(j)}$ is the SIF reference spectrum as derived in Section 2.1.1. This spectrum is scaled by C_{SIF} which is optimized in the fitting procedure and the desired result of the retrieval. The model function also includes an optional linear combination of atmospheric trace gas absorptions, $R_i(j)$, and their respective fit factors a_i in the last term. The reference spectra $R_i(j)$ are typically calculated by convoluting highly resolved literature absorption cross-sections with single atomic emission lines of Hg or Ar. Ideally, an emission line should be chosen that lies within or close to the SIF retrieval wavelength range, since the slit function is usually not constant over the entire wavelength range. For the red SIF retrieval, the Ar emission line at 696 nm is selected with a full-width-at-half-maximum (FWHM) of 0.26 nm. For the far-red SIF retrieval the Ar emission line at 763 nm with a FWHM of 0.31 nm. All mathematical procedures described here are performed within the DOASIS software package (Kraus, 2006).

To optimize the PhotoSpec retrievals for low statistical error and retrieval stability, wavelength windows that exclude strong

atmospheric absorbers, such as those from water vapor and oxygen, are selected. It should be noted that our approach can be expanded to other wavelength regions, which will be addressed in future studies.

The SIF retrieval for the red is performed in the 680–686 nm wavelength range, which is close to, but outside of the O_2-B band. This spectral region contains the Zeeman triplet Fraunhofer line Fe I at 684.3 nm, which is located close to the red emission peak of fluorescence. Weak water vapor absorption features are also present, but to a much lesser extent than the region around the Fraunhofer Hα line at 656.3 nm. Thus, the water vapor absorption cross-section is not included in the SIF spectral retrieval. There are no other narrow-band trace gas absorption features present in the chosen SIF retrieval range. A fit polynomial of 4th order is selected, and the spectra are allowed to shift in order to account for any small spectral drifts, for example due to residual temperatures instabilities.

The SIF analysis for the far-red is performed in the wavelength range 745–758 nm, which is directly next to, but outside of the strong O_2-A band around 765 nm. A fit polynomial of 4th order is chosen and the spectra are allowed to shift, similar to the SIF analysis in the red wavelength range. Ozone shows an absorption feature in this wavelength window and is thus included in the SIF spectral retrieval. The ozone absorption cross-section (Serdyuchenko et al., 2014) is convolved to the spectral resolution of the far-red spectrometer using the single Ar emission line located at 763 nm (Section 4.1). Similar to the red SIF retrieval, only very weak water vapor absorption features are present, and the water vapor absorption cross-section is thus not included in the far-red SIF spectral retrieval. If the SIF analysis wavelength range is changed or a larger amount of water vapor is present, water absorptions should be included in the SIF retrieval.

Fig. 7 shows an example for a SIF spectral retrieval in the red wavelength range. The top panel compares the logarithms of a diffuser spectrum with that observed on a tree canopy and a literature solar spectrum (Kurucz et al., 1984) convoluted with the PhotoSpec instrument function. The comparison illustrates that the main spectral structures in this wavelength range are solar Fraunhofer lines. The middle panel shows the results of the retrieval by comparing $C_{\mathrm{SIF}} \frac{R_{\mathrm{SIF}}(j)}{I^C(j)}$ (red) with the spectrum and added fit residuals (red). The comparison between the two spectra illustrates that the fit is a good approximation for $\frac{R_{\mathrm{SIF}}(j)}{I^C(j)}$ above the residuals. The bottom panel shows the residual of the fit, which is mostly noise above 681.5 nm, with a small unidentified structure below 681.5 nm. The RMS of the residual is $\sim 9 \cdot 10^{-4}$. After applying the PhotoSpec calibration, the resulting SIF signal is 2.26 ± 0.08 mW m^{-2} sr^{-1} nm^{-1}, where the error solely reflects the retrieval uncertainty.

4.3. Retrieval of vegetation indices

Differences in the surface reflectance between the blue, red, and near-infrared wavelength region of the spectra are used to derive vegetation indices to assess e.g., greenness, chlorophyll content, or leaf area index (LAI) (e.g., Porcar-Castell et al., 2014). The spectra of the PhotoSpec Flame spectrometer are used to calculate the average reflectance R_λ at a specific wavelength λ or a wavelength range $\lambda_1 : \lambda_2$. In order to retrieve the reflectance, all vegetation spectra are divided by a diffuser spectrum of the same target sequence. At this point, three vegetation indices are routinely retrieved (see Fig. 5 for mathematical equations).

The Normalized Difference Vegetation Index (NDVI) is a measure of canopy greenness (Tucker, 1979; Carlson and Ripley, 1997; Rascher et al., 2015).

The Enhanced Vegetation Index (EVI) enhances the greenness observation by correcting for structural and atmospheric effects by weighting the spectral regions differently and by taking an additional blue wavelength band into consideration (Huete et al., 1997). The Photochemical Reflectance Index (PRI) has been used to estimate dynamics in the xanthophyll pigment interconversion (e.g., Magney et al., 2016), using the reflectance at 531 nm together with a reference band at 570 nm (Gamon et al., 1992). Other vegetation indices that can be calculated from other combinations of surface reflectances between 350 and 1000 nm, will be investigated in the future, such as the Canopy Chlorophyll Content Index (CCCI) to estimate the chlorophyll content to disentangle the SIF signal from shifts in the chlorophyll

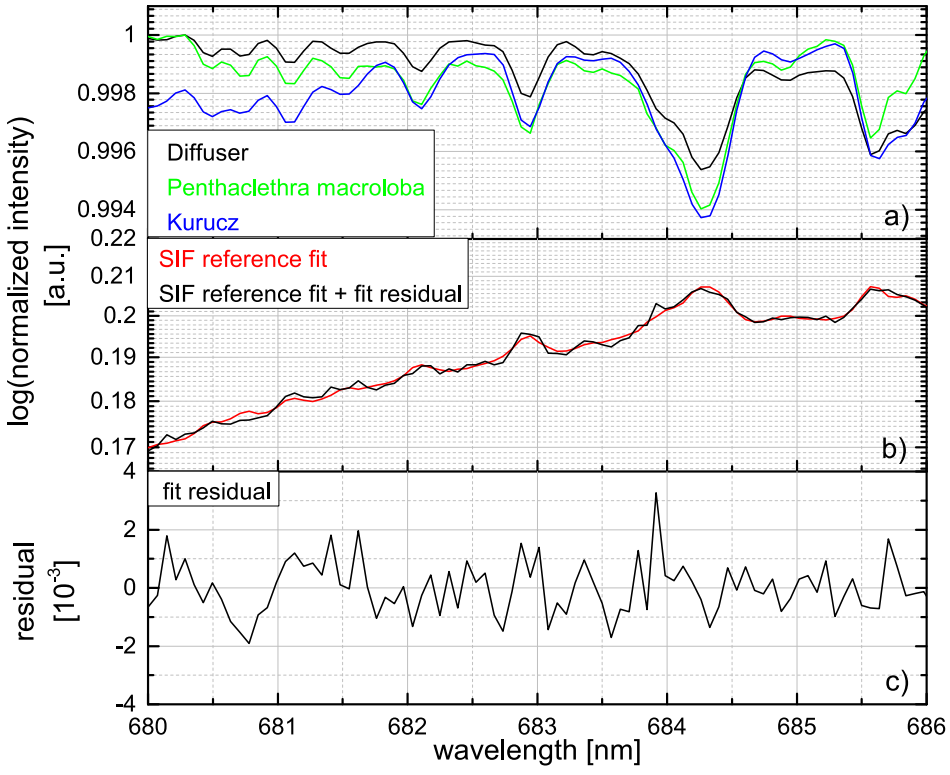

Fig. 7. Example for a SIF spectral retrieval in the red wavelength range for a *Penthaclethra macroloba* spectrum recorded on 4/21/2017 at 13:09 (LT) at an SZA of 23° and a fit RMS of $9.11 \cdot 10^{-4}$. Panel a) compares diffuser and canopy spectra with those from a solar reference (Kurucz). Panel b) shows the fit results (red) compared to the fit result with the added retrieval residual (black). The residual, i.e., the unexplained spectral structure, of the retrieval is shown in panel c). The calibrated SIF signal of this spectrum is 2.26 ± 0.08 mW m^{-2} sr^{-1} nm^{-1}.

Table 2
Errors of the retrieved SIF data.

Error type	Error source	Red	Far-red
Statistical	Retrieval error	0.05 mW m^{-2} sr^{-1} nm^{-1}	0.1 mW m^{-2} sr^{-1} nm^{-1}
	Retrieval error for a typical SIF signal	4%	5%
Systematic	Offset	10^{-3}%	10^{-5}%
	Dark current	$6 \cdot 10^{-4}$%	$6 \cdot 10^{-4}$%
	Detector nonlinearity	10^{-5}%	10^{-5}%
	Stray light	2.5%	1%[1]
	Calibration	7%	7%

[1] 11% in early PhotoSpec version.

concentration (e.g., Perry et al., 2012). As PhotoSpec records the entire spectrum from 350 to 1000 nm, we can also go beyond traditional vegetation indices in the future and take the full spectral shape into account, for instance through partial least squares (Serbin et al., 2012) or general spectral decomposition with mathematical tools such as Singular Value decomposition (SVD).

The error of the vegetation indices retrieval is small and primarily consists of the photoelectron shot noise of the Flame spectrometer, which scales proportionally to the square root of the number of sampled photons. The noise level is determined in the laboratory by recording spectra of a halogen lamp at different numbers of co-added scans. The relative noise of the Flame spectrometer is approximately 10^{-3}.

4.4. Errors and uncertainties

The SIF retrieval is subject to statistical and systematic errors. Table 2 summarizes the different errors of the retrieved SIF data. The SIF fitting procedure determines a statistical uncertainty for every spectrum (Platt and Stutz, 2008), which is approximately 0.05 and 0.1 mW m^{-2} sr^{-1} nm^{-1} for the red and far-red SIF signal, respectively. This corresponds to 4% and 5% for a typical SIF signal of 1.2 and 2 mW m^{-2} sr^{-1} nm^{-1} in the red and far-red wavelength range, respectively.

As already mentioned in Section 4.1, instrumental effects such as e.g., offset (approximately 10^{-5} counts) and DC correction (approximately $6 \cdot 10^{-6}$ counts), detector nonlinearities (10^{-5}%), or stray light in the spectrometers (2.5% in the red and 1% in the far-red wavelength range) can lead to systematic uncertainties. In addition, the radiometric calibration adds a further uncertainty to the SIF data. The uncertainty of the radiometric calibration is mainly given by the uncertainty of the Ocean Optics calibration lamp and is 7% for the red and far-red wavelength range according to the calibration certificate. The total SIF retrieval error is thus dominated by the uncertainty of the radiometric calibration and also the influence of stray light. The stray light error of the prototype far-red PhotoSpec SIF channel was estimated to be around 11% and is likely the dominant error source in the early measurements. This error is absent in the later PhotoSpec versions where a better long-pass filter was used.

5. Results and discussion

The PhotoSpec instrument was installed and tested at two different locations: on the roof of the UCLA Math Sciences building and on a 40 m tower at La Selva Biological Station in Costa Rica. On the UCLA Math Sciences roof, the SIF signal of single leaves of different plants (basil, banana, peace lily) was measured, as well as the SIF signal of grass and trees on campus. All plants were kept well-watered and had replete nutrients. The PhotoSpec was installed for long-term measurements in the rainforest of La Selva Biological Station in Costa Rica in March 2017 to monitor the photosynthetic activity of different tropical species.

The SIF measurements on the roof of the UCLA Math Sciences building were compared to field observations using a portable chlorophyll fluorometer (PAM-2500, Heinz Walz GmbH, Effeltrich, Germany) to link the SIF signal to fluorescence yields (F_t and F_m from PAM, see PAM description in supplement in Section S4).

5.1. Dark-light transition measurements

Simultaneous measurements of dark-light transitions using the PhotoSpec and PAM-2500 instruments were performed to confirm that the PhotoSpec instrument was indeed observing SIF. For this experiment, the PhotoSpec telescope was pointing onto a sample leaf of a banana plant (*Dwarf Cavendish banana*) which was carefully fixed in a horizontal position to avoid any shade. The PhotoSpec instrument was set to very short exposure times of 0.5 –1.5 s to fully resolve the fast change in light intensity. The PAM-2500 sensor head was attached to the same sample leaf. During ecophysiological fluorescence measurements in the field, the sample plants are usually darkened for 30 min to measure acute photo-inhibition (Thiele and Krause, 1994). Thus, the whole sample plant, as well as the PAM-2500 leaf clip, were covered with a black cloth for 20–30 min, and then exposed to sunlight. For the PAM-2500 measurements, no saturating light pulses were triggered, only the steady-state fluorescence yield F_t was recorded.

The red and far-red SIF signal shows the expected high initial values

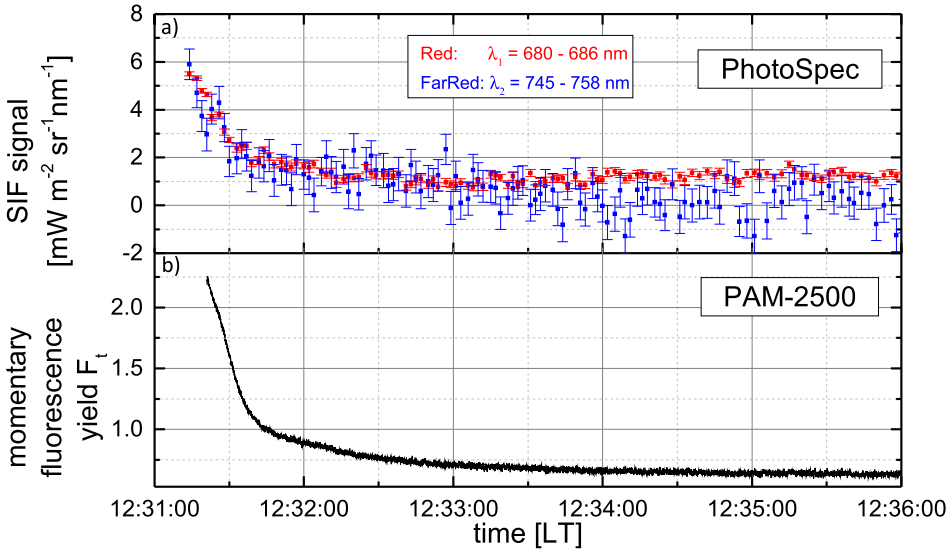

Fig. 8. Red and far-red SIF signal measured by the PhotoSpec instrument (a) and momentary fluorescence yield measured by the PAM-2500 instrument (b) of a banana leaf during a dark-light transition (Kautsky curve) on 10/18/2016. The PAR signal was 1430 μmol s^{-1} m^{-2} and did not change during the time of the Kautsky curve. It was likely < 5 μmol s^{-1} m^{-2} before when the sample plant was covered with a black cloth (not measured).

and fast decay after the dark light transition according to the Kautsky curve theory (Kautsky and Hirsch, 1931) (Fig. 8). The momentary fluorescence yield F_t measured by the fluorometer has a similar time dependence as the SIF signal. Acute photo-inhibition is reversible after 20–30 min and is due to energy dissipation via built-up of an electrochemical proton gradient across the thylakoid membranes, and via generation of heat in the xanthophyll cycle (Thiele et al., 1998). Thus, the dark-light measurement confirms that the PhotoSpec instrument does indeed detect SIF. For this measurement, the noise in the SIF signal is large due to the very short exposure times. The SIF error is larger in the far-red than in the red wavelength range, since the relative SIF signal in the red wavelength range is much larger (Section 2).

5.2. Diurnal SIF cycle

The diurnal SIF cycle of single leaves and a grass patch on UCLA's campus was investigated as examples of structurally simple conditions. All plants and grass areas on campus are irrigated. The distance between the PhotoSpec telescope and the single leaves was about 50 cm to 1 m, and the distance to the grass patch was approximately 50 m. The telescope was pointing to one specific azimuth and elevation angle on the leaf and grass patch, respectively. The telescope did not scan over the measured sample. In case of the grass patch, the PhotoSpec instrument observed an area of approximately 61 cm diameter, thus averaging over a large number of individual grass leaves. The grass was in the shade in the early morning until about 9:30 and in the late afternoon starting around 17:00 due to the surrounding buildings and trees. The single leaves were fixed in a horizontal position to avoid any shading.

Fig. 9 shows the diurnal cycle of PAR, SIF, and effective quantum yield of PSII of a peace lily (*Spathiphyllum* spp.) leaf (10/11/2016). Generally, the far-red SIF signal is larger than that in the red. The day was completely overcast in the morning and cloud free after 13:00. The transition from cloudy to sunny conditions can be observed in the simultaneous increase of the PAR and SIF signals. The morning observations show that the PhotoSpec instrument is able to measure SIF during cloudy conditions. Surprisingly, the scatter in the SIF signal appears to be smaller under the morning cloudy conditions than in the sunny afternoon, likely due to the more even canopy illumination during cloudy conditions. The scatter is also larger in the far-red than the red range, which is partially explained by the larger errors in the far-red. The effective quantum yield of PSII shows a typical diurnal cycle, with the minimum during the sunny period when the SIF signal is the largest. The levels of the effective quantum yield are overall very low because the plant was exposed to a highly stressful environment on the roof, i.e., high light and temperature, and low humidity and wind.

Fig. 10 shows the PAR, red and far-red SIF, as well as the NDVI and PRI for the grass patch on a clear day with some sparse clouds in the morning. The SIF signal generally follows the diurnal cycle of PAR. The SIF signal is lower in the early morning and late afternoon due to limiting light conditions, primarily due to the fact that the grass patch is in the shade at that time. This shade is not visible in the PAR signal as the PAR sensor is mounted on the roof of the UCLA Math Sciences building, whereas the grass patch is on the ground level surrounded by buildings and trees. The SIF signal in the far-red is approximately twice as large as in the red wavelength region, and shows more scatter than the red SIF signal. The larger far-red SIF signal is consistent with the single leaf observations. The SIF retrieval error is small, approximately 4–5 %. NDVI is constant with a value of 0.8, whereas the PRI changes during the day. The PRI often has a midday depression due to plant stress (Magney et al., 2016). However, for the grass, the PRI does not decrease at midday, likely because the grass was not water-stressed or due to changes in solar illumination angles. The fact that the SIF signal is relatively flat during peak irradiance while the PAR signal continues to increase may support previous reports that SIF is less impacted by diurnal variations in the canopy reflectivity than other vegetation indices (Damm et al., 2014).

5.3. Spatially distributed SIF at La Selva Biological Station, Costa Rica

For the first long-term field deployment, the PhotoSpec instrument was installed on a 40 m high tower at La Selva Biological Station in Costa Rica (latitude: 10.43070°N, longitude: 84.00670°W) in March 2017. La Selva Biological Station is one of the most important sites for rainforest research, with the longest annual record of tropical tree growth worldwide (e.g., Clark and Clark, 2000; Clark et al., 2013). The site typically experiences less rainfall from January to April and more rainfall from October to December (Sanford et al., 1994).

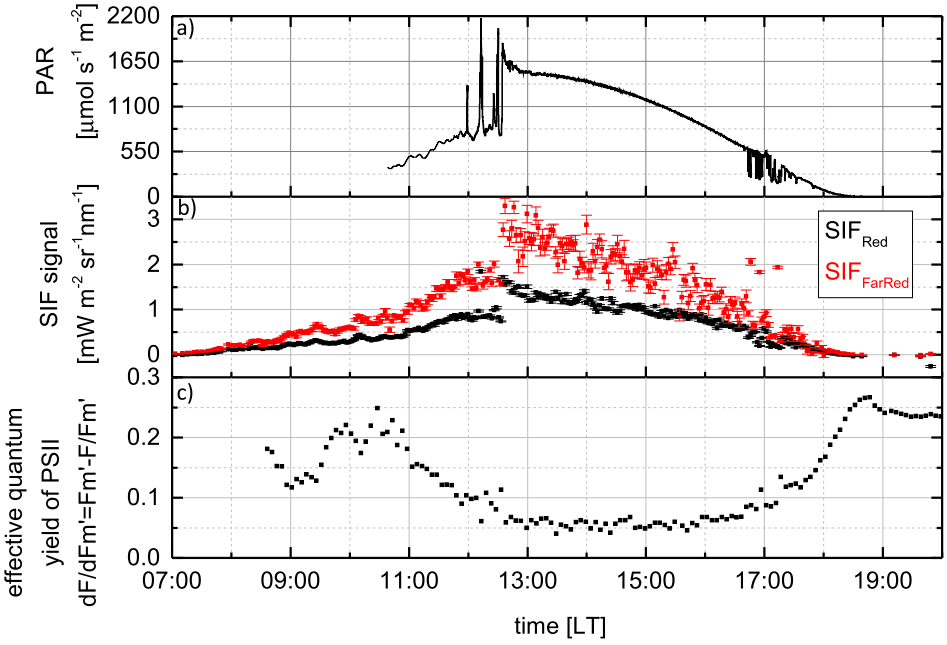

Fig. 9. Diurnal cycle of PAR (a), SIF (b), and effective quantum yield of PSII (c) of a peace lily leaf (10/11/2016). The distance between the peace lily leaf and the PhotoSpec telescope is approximately 1 m.

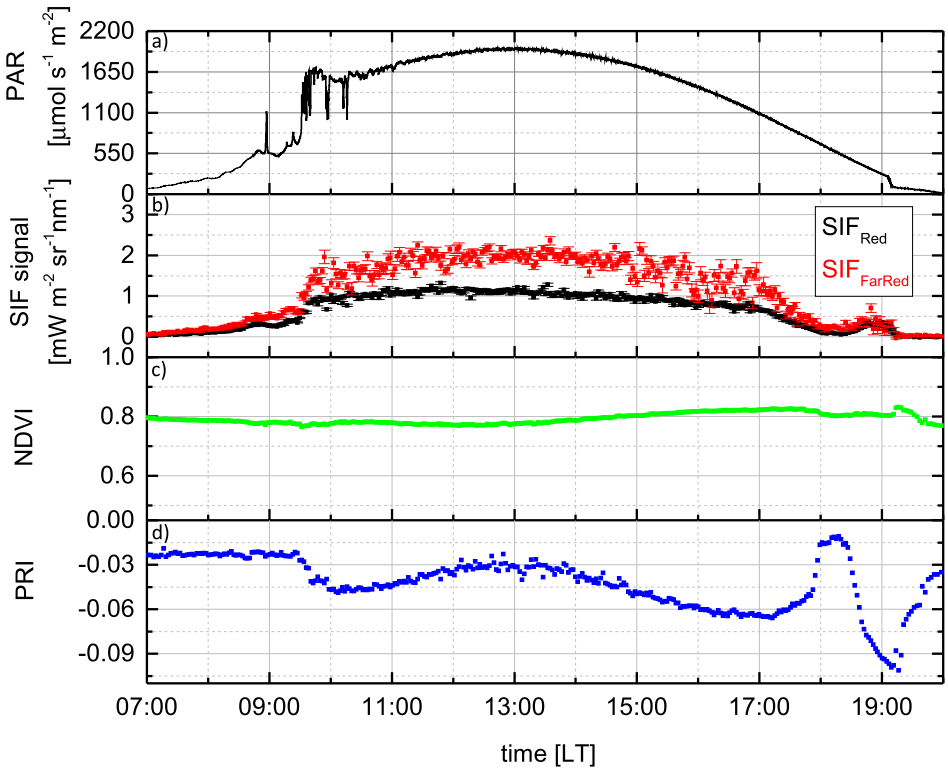

Fig. 10. Diurnal cycle of PAR (a), SIF (b), NDVI (c), and PRI (d) of a grass patch on the UCLA campus (07/16/2016). The distance between grass patch and PhotoSpec telescope is approximately 50 m. The illumination conditions change throughout the day. The grass patch was in the shade in the early morning and late afternoon due to the surrounding buildings and trees.

Since March 2017, the PhotoSpec instrument has monitored different tree species at La Selva. Of particular interest is the species *Pentaclethra macroloba*, a leguminous tree which constitutes 37% of the aboveground biomass in the rainforest (Clark and Clark, 2000). *Pentaclethra macroloba* often occupies the upper canopy layer directly underneath the top of the trees, i.e., in an environment that is not too shaded and not too exposed. The leaves are highly productive, providing promising targets for SIF measurements.

The PhotoSpec instrument is performing different scanning strategies, with a total integration time of 30 s per spectrum. Every second day, the 2D scanning telescope unit is pointing towards 22 individual targets around the tower. On the other days, raster scans are performed over two species, *Penthaclethra macroloba* and *Vismia macrophylla*, as well as elevation scans from a nadir viewing direction to the horizon across the canopy at a fixed azimuth angle.

Fig. 11 shows a typical diurnal cycle during the target scanning sequence for five exemplary targets (top to bottom rows: *Penthaclethra macroloba*($\alpha = -44°$), *Vismia macrophylla* ($\alpha = -67°$), *Castilla elastica* ($\alpha = -70°$), *Dussia macrophyllata* ($\alpha = -15°$), *Philodendron radiatum* ($\alpha = -25°$)) at La Selva Biological Station on 4/21/2017. The red and far-red SIF signals (second column) directly correlate with the intensity in the red and far-red wavelength range (left column), respectively. The early morning was characterized by clear skies, followed by broken cloud cover between 9:00 and 12:00. The afternoon was again mostly cloud free. The intensity and SIF signal of *Penthaclethra macroloba* and *Dussia macrophyllata* reflect this pattern, showing a smooth increase until 9:00, a highly variable SIF and intensity from 9:00 to 12:00, and an increase after noon when the plant was exposed to full sunlight. The diurnal SIF and intensity profiles of the other species are more variable since their leaves are more shaded.

The dominant role of solar radiance reaching the observed area in the canopy for SIF diurnal variations is also evident in the much smoother relative SIF signal (third column). The relative SIF signals, i.e., the SIF signal relative to the average intensity in the respective wavelength range, are in the range of 0.01–0.04 in the far-red and 0.05–0.3 in the red. The very high relative SIF in the red is a consequence of the chlorophyll absorption in the canopy. The SIF signal in the red and far-red wavelength range is similar for some species (*Vismia macrophylla*, *Castilla elastica*), but different for the other species, which is due to PSI/PSII modifications in the spectral shape over the diurnal timescale and chlorophyll content on the seasonal time scale. This observations will be explored in forthcoming publications. The ratio between the red and far-red SIF depends on the viewing geometry, and is close to one for nadir viewing direction, and smaller than one for an elevation angle close to the horizon. Detailed radiative transfer considerations are needed to verify if this is a common behavior of SIF observations.

The NDVI for all sampled species (fourth row) is about 0.9 and varies slightly by 0.05. The PRI varies with the incoming sunlight, and shows a diurnal cycle with a minimum in the afternoon, as observed in other studies (e.g., Magney et al., 2016). The PRI also reflects the variation in solar radiation during the cloudy period between 9:00 and 12:00.

While a detailed exploration of the observed SIF signals goes beyond the scope of this technical instrument paper, the examples presented in the sections above illustrate the potential of PhotoSpec data to advance our understanding of SIF in natural and agricultural canopies. The spatial scanning capability distinguishes PhotoSpec from other available SIF instruments, which typically use bare fibers and thus fixed, wide, FOVs. Other tower-based SIF instruments, e.g., the FluoSpec (Yang et al., 2015), MRI and SFLUOR box (Cogliati et al., 2015a), and FLOX system (http://jb-hyperspectral.com), have a dual FOV, one pointing towards the canopy with a FOV of 25°, while the other is pointing onto a cosine corrector. With the 2D scanning telescope unit and the small FOV of the PhotoSpec instrument, not only are single leaf measurements possible, but also spatial raster scans over the whole canopy. The step size can be as small as the FOV itself, i.e., an average over a canopy scan can be compared to airborne and satellite data. From this, detailed statistical analyses can be performed to provide more information about the variation within the canopy. Measurements of trunks, soil, and branches can be both excluded and included from the scans during analysis to represent the canopy averages of non-

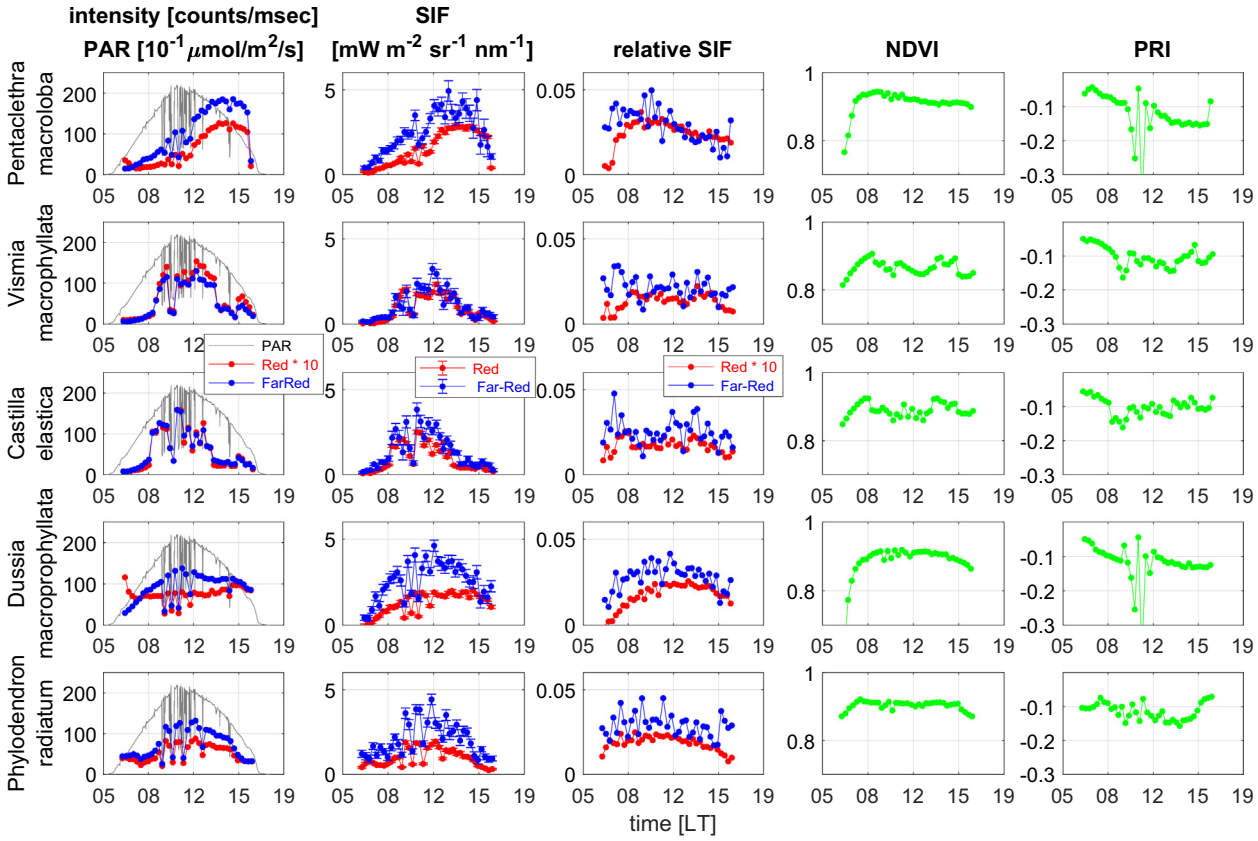

Fig. 11. Diurnal cycle of intensity and PAR (column 1), SIF (column 2), relative SIF (column 3), NDVI (column 4), and PRI (column 5) of five different species at La Selva on 4/21/2017 (SZA < 75°, α= elevation viewing angle): *Penthaclethra macroloba* ($\alpha = -44°$, row 1), *Vismia macrophyllata* ($\alpha = -67°$, row 2), *Castilla elastica* ($\alpha = -70°$, row 3), *Dussia macrophyllata* ($\alpha = -15°$, row 4), *Phylodendron radiatum* ($\alpha = -25°$, row 5). The intensity of the *Dussia macrophyllata* in the red wavelength range has a peak in the morning during clear days. This peak, which disappears during cloudy periods, will be studied in the future.

photosynthetic and photosynthetic canopy components (see Figure S3 in the supplement as an example for a non-fluorescence target, which has a SIF signal of zero). This will provide more information about the variation within the canopy, and improved understanding of contributions of everything within a canopy FOV (i.e., satellite).

6. Conclusions

We have developed an automated remote sensing system – PhotoSpec - for simultaneous measurements of red and far-red SIF as well as vegetation indices. The combination of red and far-red SIF observations offers unique opportunities to study photosynthesis in a complex canopy, for example allowing us to gather information on SIF re-absorption in the red wavelength range in different layers of a canopy, as well as to study of the responses to environmental stress factors.

The instrument is designed for highly stable and sensitive operations using the principle of the in-filling of solar Fraunhofer lines, as also used for satellite SIF retrievals as well as for some ground-based SIF measurements. SIF retrievals using the in-filling of solar Fraunhofer lines have the advantage that they are less affected by clouds and aerosols since the spectral structure of solar Fraunhofer lines is not modified by atmospheric phenomena, as is the case with atmospheric oxygen absorption features (Joiner et al., 2011; Frankenberg et al., 2011a). Consequently, the PhotoSpec instrument has the ability to detect SIF during cloudy conditions.

The stability of PhotoSpec and the use of Fraunhofer line in-filling allows the use of a fast linear least square fit approach to determine the SIF signal. We selected the most simple linearized least square retrieval approach for the standard PhotoSpec analysis. More detailed investigations in the future will reveal if this conclusion holds true for long-term datasets.

For the red SIF retrieval, we developed a novel two-step linearized analysis method to overcome the approximation limitations of the linearization due to the much lower canopy reflectivity in the red wavelength range. The retrieval approach allows data to be processed in real-time. The relative error of the red and far-red SIF retrieval of approximately 4–5 % is very low. The main uncertainty of the overall SIF signal is due to the uncertainty of the radiometric calibration. An improved radiometric calibration will be implemented in future versions.

The PhotoSpec system was designed to provide spatial canopy scans and probe various plants with one single instrument using a newly developed 2D scanning telescope unit with a narrow field of view of 0.7°. A special feature of the optical design is that simultaneous co-centered observations of red and far-red SIF as well as vegetation indices are possible. The spatial scanning strategies can be adapted to investigate various open questions on the interpretation and use of SIF, including the behavior of individual plant species, the impact of radiative transfer conditions in the canopy on SIF, etc.

First tests of the PhotoSpec instrument, in combination with measurements using the PAM-2500 fluorometer, show that the PhotoSpec is indeed able to sensitively detect SIF under various conditions. Flux-tower based PhotoSpec observations will provide unique datasets on photosynthetic activity of natural and agricultural ecosystem continuously and at high temporal resolution to bridge the gap between leaf, canopy, and satellite SIF observations, for example to investigate the impact of environmental stress on photosynthetic processes and CO_2 exchange.

Acknowledgments

This work is funded in part by the W.M. Keck Institute for Space Studies and internal funds from the Jet Propulsion Laboratory (http://www.kiss.caltech.edu/study/photosynthesis/technology.html). The authors would like to thank A. Pivovaroff (La Kretz Center for California Conservation Science, University of California Los Angeles, Los Angeles, CA, USA) for the assistance with the PAM-2500 measurements of single leaves on the UCLA Math Sciences building in 2016. The research project at La Selva Biological Station, Costa Rica, is supported by the NSF Career award (grant # 1455381) and the ECTS-R (Emerging Challenges in Tropical Science-Research) research fellowship provided by the Organization for Tropical Studies (OTS). The authors would like to thank the OTS staff at La Selva, especially D. Dierick, for their continuous help and support with the PhotoSpec installation and maintenance.

Appendix A. Supplementary data

Supplementary data to this article can be found online at https://doi.org/10.1016/j.rse.2018.07.002.

References

Agati, G., Cerovic, Z., Moya, I., 2000. The effect of decreasing temperature up to chilling values on the in vivo F685/F735 chlorophyll fluorescence ratio in *Phaseolus vulgaris* and *Pisum sativum*: the role of the photosystem i contribution to the 735 nm fluorescence band. Photochem. Photobiol. 72 (1), 75–84 (July).

Baker, N.R., 2008. Chlorophyll fluorescence: a probe of photosynthesis in vivo. Annu. Rev. Plant Biol. 59 (1), 89–113.

Bodhaine, B.A., Wood, N.B., Dutton, E.G., Slusser, J.R., 1999. On Rayleigh optical depth calculations. J. Atmos. Oceanic Technol. 16 (11), 1854–1861.

Burkart, A., Cogliati, S., Schickling, A., Rascher, U., 2014. A novel UAV-based ultra-light weight spectrometer for field spectroscopy. IEEE Sensors J. 14 (1), 62–67.

Carlson, T.N., Ripley, D.A., 1997. On the relation between NDVI, fractional vegetation cover, and leaf area index. Remote Sens. Environ. 62 (3), 241–252.

Chance, K., Kurucz, R., 2010. An improved high-resolution solar reference spectrum for earth's atmosphere measurements in the ultraviolet, visible, and near infrared. J. Quant. Spectrosc. Radiat. Transf. 111, 1289–1295.

Clark, D., Clark, D., 2000. Landscape-scale variation in forest structure and biomass in a tropical rain forest. For. Ecol. Manag. 137 (1-3), 185–198.

Clark, D.A., Clark, D.B., Oberbauer, S.F., 2013. Field-quantified responses of tropical rainforest aboveground productivity to increasing CO_2 and climatic stress, 1997–2009. J. Geophys. Res. Biogeosci. 118 (2), 783–794.

Cogliati, S., Rossini, M., Julitta, T., Meroni, M., Schickling, A., Burkart, A., Pinto, F., Rascher, U., Colombo, R., 2015a. Continuous and long-term measurements of reflectance and sun-induced chlorophyll fluorescence by using novel automated field spectroscopy systems. Remote Sens. Environ. 164, 270–281.

Cogliati, S., Verhoef, W., Kraft, S., Sabater, N., Alonso, L., Vicent, J., Moreno, J., Drusch, M., Colombo, R., 2015b. Retrieval of sun-induced fluorescence using advanced spectral fitting methods. Remote Sens. Environ. 169, 344–357.

Damm, A., Guanter, L., Laurent, V., Schaepman, M., Schickling, A., Rascher, U., 2014. FLD-based retrieval of sun-induced chlorophyll fluorescence from medium spectral resolution airborne spectroscopy data. Remote Sens. Environ 147 (Supplement C), 256–266.

Damm, A., Guanter, L., Paul-Limoges, E., van der Tol, C., Hueni, A., Buchmann, N., Eugster, W., Ammann, C., Schaepman, M., 2015. Far-red sun-induced chlorophyll fluorescence shows ecosystem-specific relationships to gross primary production: an assessment based on observational and modeling approaches. Remote Sens. Environ. 166, 91–105.

Du, S., Liu, L., Liu, X., Hu, J., 2017. Response of canopy solar-induced chlorophyll fluorescence to the absorbed photosynthetically active radiation absorbed by chlorophyll. Remote Sens. 9 (9).

Frankenberg, C., Butz, A., Toon, G.C., Frankenberg, C., Butz, A., Toon, G.C., 2011a. Disentangling chlorophyll fluorescence from atmospheric scattering effects in O_2 a-band spectra of reflected sun-light. Geophys. Res. Lett. 38 (3), l03801.

Frankenberg, C., Fisher, J.B., Worden, J., Badgley, G., Saatchi, S.S., Lee, J.E., Toon, G.C., Butz, A., Jung, M., Kuze, A., Yokota, T., 2011b. New global observations of the terrestrial carbon cycle from GOSAT: patterns of plant fluorescence with gross primary productivity. Geophys. Res. Lett. 38 (17), l17706.

Frankenberg, C., O'Dell, C., Berry, J., Guanter, L., Joiner, J., Köhler, P., Pollock, R., Taylor, T.E., 2014. Prospects for chlorophyll fluorescence remote sensing from the orbiting carbon observatory-2. Remote Sens. Environ. 147, 1–12.

Frankenberg, C., O'Dell, C., Guanter, L., McDuffie, J., Frankenberg, C., O'Dell, C., Guanter, L., McDuffie, J., 2012. Remote sensing of near-infrared chlorophyll fluorescence from space in scattering atmospheres: implications for its retrieval and interferences with atmospheric CO_2 retrievals. Atmos. Meas. Tech. 5 (8), 2081–2094.

Fraunhofer, J., 1817. Bestimmung des Brechungs- und des farbenzerstreungs-vermögens verschiedener glasarten, in Bezug auf die Vervollkommnung achromatischer Fernröhre. Ann. Phys. 56 (7), 264–313.

Gamon, J., Peñuelas, J., Field, C., 1992. A narrow-waveband spectral index that tracks diurnal changes in photosynthetic efficiency. Remote Sens. Environ. 41 (1), 35–44.

Genty, B., Briantais, J.-M., Baker, N.R., 1989. The relationship between the quantum yield of photosynthetic electron transport and quenching of chlorophyll fluorescence. Biochim. Biophys. Acta 990 (1), 87–92.

Genty, B., Wonders, J., Baker, N.R., 1990. Non-photochemical quenching of Fo in leaves is emission wavelength dependent: consequences for quenching analysis and its interpretation. Photosynth. Res. 26 (2), 133–139.

Gitelson, A.A., Buschmann, C., Lichtenthaler, H.K., 1999. The chlorophyll fluorescence ratio F735/F700 as an accurate measure of the chlorophyll content in plants. Remote Sens. Environ. 69 (3), 296–302.

Gitelson, A.A., Merzlyak, M.N., 1997. Remote estimation of chlorophyll content in higher plant leaves. Int. J. Remote Sens. 18 (12), 2691–2697.

Guanter, L., Frankenberg, C., Dudhia, A., Lewis, P.E., Gómez-Dans, J., Kuze, A., Suto, H., Grainger, R.G., 2012. Retrieval and global assessment of terrestrial chlorophyll fluorescence from GOSAT space measurements. Remote Sens. Environ. 121, 236–251.

Guanter, L., Rossini, M., Colombo, R., Meroni, M., Frankenberg, C., Lee, J.E., Joiner, J., 2013. Using field spectroscopy to assess the potential of statistical approaches for the retrieval of sun-induced chlorophyll fluorescence from ground and space. Remote Sens. Environ. 133, 52–61.

Hilker, T., Gitelson, A., Coops, N.C., Hall, F.G., Black, T.A., 2011. Tracking plant physiological properties from multi-angular tower-based remote sensing. Oecologia 165 (4), 865–876.

Huete, A., Liu, H., Batchily, K., van Leeuwen, W., 1997. A comparison of vegetation indices over a global set of TM images for EOS-MODIS. Remote Sens. Environ. 59 (3), 440–451.

Joiner, J., Guanter, L., Lindstrot, R., Voigt, M., Vasilkov, A.P., Middleton, E.M., Huemmrich, K.F., Yoshida, Y., Frankenberg, C., 2013. Global monitoring of terrestrial chlorophyll fluorescence from moderate-spectral-resolution near-infrared satellite measurements: methodology, simulations, and application to GOME-2. Atmos. Meas. Tech. 6 (10), 2803–2823.

Joiner, J., Yoshida, Y., Vasilkov, A.P., Middleton, E.M., Campbell, P.K.E., Yoshida, Y., Kuze, A., Corp, L.A., 2012b. Filling-in of near-infrared solar lines by terrestrial fluorescence and other geophysical effects: simulations and space-based observations from SCIAMACHY and GOSAT. Atmos. Meas. Tech. 5 (4), 809–829.

Joiner, J., Yoshida, Y., Vasilkov, A.P., Yoshida, Y., Corp, L.A., Middleton, E.M., 2011. First observations of global and seasonal terrestrial chlorophyll fluorescence from space. Biogeosciences 8 (3), 637–651.

Kautsky, H., Hirsch, A., 1931. Neue Versuche zur Kohlensäureassimilation. Naturwissenschaften 19 (48) 964–964 (Nov).

Kirchhoff, G., 1860. Ueber das Verhältniss zwischen dem Emissionsvermögen und dem Absorptionsvermögen der Körper für Wärme und Licht. Ann. Phys. 185 (2), 275–301.

Köhler, P., Guanter, L., Joiner, J., 2015. A linear method for the retrieval of sun-induced chlorophyll fluorescence from GOME-2 and SCIAMACHY data. Atmos. Meas. Tech. 8 (6), 2589–2608.

Kraus, S.G., 2006. DOASIS: A Framework Design for DOAS. Ph.D. thesis. University of Mannheim.

Krause, G., Weis, E., 1991. Chlorophyll fluorescence and photosynthesis: the basics. Ann. Rev. Plant Phys. Plant Mol. Biol. 42 (1), 313–349.

Kurucz, R.L., Furenlid, I., Brault, J., Testerman, L., 1984. Solar flux atlas from 296 to 1300 nm. In: Tech. Rep. National Solar Observatory.

Lee, J.E., Frankenberg, C., van der Tol, C., Berry, J.A., Guanter, L., Boyce, C.K., Fisher, J.B., Morrow, E., Worden, J.R., Asefi, S., Badgley, G., Saatchi, S., 2013. Forest productivity and water stress in Amazonia: observations from GOSAT chlorophyll fluorescence. Proc. R. Soc. Lond. B Biol. Sci. 280 (1761).

Liu, L., Liu, X., Wang, Z., Zhang, B., 2016. Measurement and analysis of bidirectional SIF emissions in wheat canopies. IEEE Trans. Geosci. Remote Sens. 54 (5), 2640–2651 (May).

Magney, T.S., Frankenberg, C., Fisher, J.B., Sun, Y., North, G.B., Davis, T.S., Kornfeld, A., Siebke, K., 2017. Connecting active to passive fluorescence with photosynthesis: a method for evaluating remote sensing measurements of Chl fluorescence. New Phytol. 2017–23758.

Magney, T.S., Vierling, L.A., Eitel, J.U., Huggins, D.R., Garrity, S.R., 2016. Response of high frequency photochemical reflectance index (PRI) measurements to environmental conditions in wheat. Remote Sens. Environ. 173, 84–97.

Meroni, M., Rossini, M., Guanter, L., Alonso, L., Rascher, U., Colombo, R., Moreno, J., 2009. Remote sensing of solar-induced chlorophyll fluorescence: review of methods and applications. Remote Sens. Environ. 113 (10), 2037–2051.

Middleton, E., Rascher, U., Corp, L., Huemmrich, K., Cook, B., Noormets, A., Schickling, A., Pinto, F., Alonso, L., Damm, A., Guanter, L., Colombo, R., Campbell, P., Landis, D., Zhang, Q., Rossini, M., Schuettemeyer, D., Bianchi, R., 2017. The 2013 FLEX - US airborne campaign at the Parker Tract Loblolly Pine Plantation in North Carolina, USA. Remote Sens. 9, 612 (Jun.).

Moya, I., Camenen, L., Evain, S., Goulas, Y., Cerovic, Z., Latouche, G., Flexas, J., Ounis, A., 2004. A new instrument for passive remote sensing: 1. measurements of sunlight-induced chlorophyll fluorescence. Remote Sens. Environ. 91 (2), 186–197.

Moya, I., Camenen, L., Latouche, G., Mauxion, C., Evain, S., Cerovic, Z., 1998. An Instrument for the Measurement of Sunlight Excited Plant Fluorescence. Springer, Dordrecht.

Perry, E.M., Fitzgerald, G.J., Nuttall, J.G., O'Leary, G.J., Schulthess, U., Whitlock, A., 2012. Rapid estimation of canopy nitrogen of cereal crops at paddock scale using a canopy chlorophyll content index. Field Crop Res. 134, 158–164.

Plascyk, J.A., Gabriel, F.C., 1975. The Fraunhofer line discriminator MKII - an airborne instrument for precise and standardized ecological luminescence measurement. IEEE

Trans. Instrum. Meas. 24 (4), 306–313 (Dec).
Platt, U., Stutz, J., 2008. Differential Optical Absorption Spectroscopy: Principles and Applications. Springer Verlag Berlin Heidelberg.
Porcar-Castell, A., Tyystjärvi, E., Atherton, J., van der Tol, C., Flexas, J., Pfündel, E.E., Moreno, J., Frankenberg, C., Berry, J.A., 2014. Linking chlorophyll a fluorescence to photosynthesis for remote sensing applications: mechanisms and challenges. J. Exp. Bot. 65 (15), 4065–4095.
Rascher, U., Agati, G., Alonso, L., Cecchi, G., Champagne, S., Colombo, R., Damm, A., Daumard, F., de Miguel, E., Fernandez, G., Franch, B., Franke, J., Gerbig, C., Gioli, B., Gómez, J.A., Goulas, Y., Guanter, L., Gutiérrez-de-la Cámara, O., Hamdi, K., Hostert, P., Jiménez, M., Kosvancova, M., Lognoli, D., Meroni, M., Miglietta, F., Moersch, A., Moreno, J., Moya, I., Neininger, B., Okujeni, A., Ounis, A., Palombi, L., Raimondi, V., Schickling, A., Sobrino, J.A., Stellmes, M., Toci, G., Toscano, P., Udelhoven, T., van der Linden, S., Zaldei, A., 2009. CEFLES2: the remote sensing component to quantify photosynthetic efficiency from the leaf to the region by measuring sun-induced fluorescence in the oxygen absorption bands. Biogeosciences 6 (7), 1181–1198.
Rascher, U., Alonso, L., Burkart, A., Cilia, C., Cogliati, S., Colombo, R., Damm, A., Drusch, M., Guanter, L., Hanus, J., Hyvärinen, T., Julitta, T., Jussila, J., Kataja, K., Kokkalis, P., Kraft, S., Kraska, T., Matveeva, M., Moreno, J., Muller, O., Panigada, C., Pikl, M., Pinto, F., Prey, L., Pude, R., Rossini, M., Schickling, A., Schurr, U., Schüttemeyer, D., Verrelst, J., Zemek, F., 2015. Sun-induced fluorescence - a new probe of photosynthesis: first maps from the imaging spectrometer hyplant. Glob. Chang. Biol. 21 (12), 4673–4684.
Rossini, M., Nedbal, L., Guanter, L., Ač, A., Alonso, L., Burkart, A., Cogliati, S., Colombo, R., Damm, A., Drusch, M., Hanus, J., Janoutova, R., Julitta, T., Kokkalis, P., Moreno, J., Novotny, J., Panigada, C., Pinto, F., Schickling, A., Schüttemeyer, D., Zemek, F., Rascher, U., 2015. Red and far red sun-induced chlorophyll fluorescence as a measure of plant photosynthesis. Geophys. Res. Lett. 42 (6), 1632–1639 2014GL062943.
Sanford, J., Paaby, P., Luvall, J.C., Phillips, E., 1994. Climate, Geomorphology, and Aquatic Systems in La Selva: Ecology and Natural History of a Neotropical Rain Forest. University of Chicago Press, Chicago, Illinois, pp. 19–33.
Serbin, S.P., Dillaway, D.N., Kruger, E.L., Townsend, P.A., 2012. Leaf optical properties reflect variation in photosynthetic metabolism and its sensitivity to temperature. J. Exp. Bot. 63 (1), 489–502.
Serdyuchenko, A., Gorshelev, V., Weber, M., Chehade, W., Burrows, J.P., 2014. High spectral resolution ozone absorption cross-sections - part 2: temperature dependence. Atmos. Meas. Tech. 7 (2), 625–636.
Stutz, J., Platt, U., 1996. Numerical analysis and estimation of the statistical error of differential optical absorption spectroscopy measurements with least-squares methods. Appl. Opt. 35 (30), 6041–6053.
Sun, Y., Frankenberg, C., Jung, M., Joiner, J., Guanter, L., Köhler, P., Magney, T., 2018. Overview of solar-induced chlorophyll fluorescence (SIF) from the orbiting carbon observatory-2: retrieval, cross-mission comparison, and global monitoring for GPP. Remote Sens. Environ. 209, 808–823.
Sun, Y., Frankenberg, C., Wood, J.D., Schimel, D.S., Jung, M., Guanter, L., Drewry, D.T., Verma, M., Porcar-Castell, A., Griffis, T.J., Gu, L., Magney, T.S., Köhler, P., Evans, B., Yuen, K., 2017. OCO-2 advances photosynthesis observation from space via solar-induced chlorophyll fluorescence. Science 358 (6360).
Sun, Y., Fu, R., Dickinson, R., Joiner, J., Frankenberg, C., Gu, L., Xia, Y., Fernando, N., 2015. Drought onset mechanisms revealed by satellite solar-induced chlorophyll fluorescence: insights from two contrasting extreme events. J. Geophys. Res. Biogeosci. 120 (11), 2427–2440.
Thiele, A., Krause, G.H., 1994. Xanthophyll cycle and thermal energy dissipation in photosystem II: relationship between zeaxanthin formation, energy-dependent fluorescence quenching and photoinhibition. J. Plant Physiol. 144 (3), 324–332.
Thiele, A., Krause, G.H., Winter, K., 1998. In situ study of photoinhibition of photosynthesis and xanthophyll cycle activity in plants growing in natural gaps of the tropical forest. Funct. Plant Biol. 25 (2), 189–195.
Tucker, C.J., 1979. Red and photographic infrared linear combinations for monitoring vegetation. Remote Sens. Environ. 8 (2), 127–150.
Wolanin, A., Rozanov, V., Dinter, T., Noël, S., Vountas, M., Burrows, J., Bracher, A., 2015. Global retrieval of marine and terrestrial chlorophyll fluorescence at its red peak using hyperspectral top of atmosphere radiance measurements: feasibility study and first results. Remote Sens. Environ. 166, 243–261.
Yang, H., Yang, X., Zhang, Y., Heskel, M.A., Lu, X., Munger, J.W., Sun, S., Tang, J., 2017. Chlorophyll fluorescence tracks seasonal variations of photosynthesis from leaf to canopy in a temperate forest. Glob. Chang. Biol. 23 (7), 2874–2886.
Yang, X., Tang, J., Mustard, J.F., Lee, J.E., Rossini, M., Joiner, J., Munger, J.W., Kornfeld, A., Richardson, A.D., 2015. Solar-induced chlorophyll fluorescence that correlates with canopy photosynthesis on diurnal and seasonal scales in a temperate deciduous forest. Geophys. Res. Lett. 42 (8), 2977–2987.
Zhang, Y., Guanter, L., Berry, J.A., Joiner, J., van der Tol, C., Huete, A., Gitelson, A., Voigt, M., Köhler, P., 2014. Estimation of vegetation photosynthetic capacity from space-based measurements of chlorophyll fluorescence for terrestrial biosphere models. Glob. Chang. Biol. 20 (12), 3727–3742.
Zhang, Y., Guanter, L., Berry, J.A., van der Tol, C., Yang, X., Tang, J., Zhang, F., 2016. Model-based analysis of the relationship between sun-induced chlorophyll fluorescence and gross primary production for remote sensing applications. Remote Sens. Environ. 187, 145–155.